Causes of marine heatwaves in the East China Sea and the South Yellow Sea in three consecutive summers during 2016-2018

Guandong Gao[1,2,3], Maxime Marin[4,5], Ming Feng[4]*, Baoshu Yin[1,2,3,6]*, Dezhou Yang[1,2,3], Xingru Feng[1,2,3], Yang Ding[7,2], Dehai Song[7,2]

[1] Key Laboratory of Ocean Circulation and Waves, Institute of Oceanology Chinese Academy of Sciences, Qingdao 266071, China

[2] Qingdao National Laboratory for Marine Science and Technology, Qingdao 266000, China

[3] Center for Mega Science, Chinese Academy of Science, 7 Nanhai Road, Qingdao, 266071, P. R. China

[4] CSIRO Oceans and Atmosphere, Crawley, Western Australia, Australia,

[5] Institute for Marine and Antarctic Studies, University of Tasmania, Hobart, Tasmania, Australia,

[6] University of Chinese Academy of Sciences, Beijing 100049, China.

[7] Key Laboratory of Physical Oceanography, Ministry of Education, at Ocean University of China, Qingdao 266100, China

24 *Corresponding author: Ming Feng

25 E-mail address: ming.feng@csiro.au

26 *Corresponding author: Baoshu Yin

27 E-mail address: bsyin@qdio.ac.cn

Abstract

In three consecutive years from 2016 to 2018, extreme ocean warming events, or marine heatwaves (MHW), occurred during boreal summers in the East China Sea (ECS) and South Yellow Sea (SYS), which was unprecedented in the past four decades based on the satellite record. In this study, we used a high-resolution hydrodynamic model based on FVCOM (Finite Volume Community Ocean Model) to simulate the evolution of these warming events. An upper ocean temperature budget (0-20m) analysis based on the model results shows that the shortwave radiation and the ocean advection anomalies jointly contributed to the anomalous warming in the three successive summers (June-August) in the SYS and the north part of the ECS. In addition, the reduction of surface wind speeds during the 2016 and 2017 summers further weakened the vertical mixing, thereby enhancing the anomalous warming in the north part of the ECS adjacent to the SYS. During the three summers, the increases of shortwave radiation were closely related to the East Asian Summer Monsoon variability, which reduced the cloud cover in the ECS and SYS, whereas the advection anomalies were mostly associated with regional wind anomalies. In summer 2018, upper ocean heat was transported into the central trough of the South Yellow Sea, accumulated in an anticyclonic eddy generated by the anomalous wind stress curls. Understanding the drivers of the MHWs can help MHW predictions in the coastal region, in order to help the fisheries and aquaculture industries to better manage the environmental risks under a warming climate.

Plain language Summary

Marine heatwaves, known as periods of extreme warming at the sea surface, can last for days to months and cause damages to marine environment and marine life. In the East China Sea and the South Yellow Sea, the frequent occurrences of harmful algae bloom are often associated with marine heatwaves. Satellite data reveals that marine

heatwaves occurred in the East China Sea and the South Yellow Sea during the three boreal summers from 2016 to 2018, which were unprecedented in the past four decades. Using a numerical model of the ocean, we reproduced the marine heatwaves during these three successive summers. We show that the increased solar radiation, ocean current anomalies and reduced vertical mixing were three critical factors for the warming events in the three summers. This study is of significance to the prediction of marine heatwaves in East China Sea and the South Yellow Sea, to help the fisheries and aquaculture industries to better manage the environmental risks under a warming climate.

Key points

- Marine heatwaves in the ECS and SYS during 2016-2018 summers were caused by shortwave radiation, current and vertical mixing anomalies
- Shortwave radiation increases in summers were due to reduction of cloud cover, closely related to the East Asian Summer Monsoon variability
- An anticyclonic eddy in SYS in summer 2018, driven by regional wind anomalies, played a significant role in trapping anomalous heat

1. Introduction

The occurrences of extreme warming events in the world oceans, the marine heatwaves (MHW; Hobday et al., 2016), are becoming more frequent in the recent decade. There have been record MHW events in coastal waters off Australia (Benthuysen et al., 2014; Oliver et al., 2017; Benthuysen et al., 2018), the northern Mediterranean Sea (Sparnocchia et al., 2006; Olita et al., 2006), the northwest Atlantic (Chen et al., 2014), the northeast Pacific (Bond et al., 2015; Di Lorenzo and Mantua, 2016), and Coastal waters off South African (Schlegel et al., 2017). MHW events have drawn great attentions due to their extraordinary influences on the regional biodiversity and mortality of commercial fisheries (Mills et al., 2012; Caputi et a., 2016; Oliver et al., 2017).

There have also been observations of extreme MHW events occurring in the East China Sea (ECS; Tan and Cai et al., 2018), and the Yellow Sea in recent years. As a marginal sea of the Pacific Ocean, the ECS is connected to the South Yellow Sea (SYS) to the north (along a section from the mouth of Changjiang River, China to Jeju Island, Korea), and is separated from the South China Sea and the Philippine Sea by the Taiwan Strait and the Ryukyu Islands (Figure 1). The ECS and the SYS are known as one of the most developed continental shelf areas globally (Yanagi and Takahashi, 1993), and they are referred to as the ECS system (ECSs) in this study.

In the ECSs, the frequent occurrences of harmful algae bloom are associated to anomalous warm conditions, or marine heatwaves (Cai et al., 2016). The anomalous warming would enhance stratification and restrict phytoplankton presence in the top of water column where more light is available for them to thrive. In addition, anomalous warming in late spring and early summer greatly reduces the abundance of warm-water species of zooplankton like *C.sinicus*, which in turn reduces grazing pressure on phytoplankton and stimulates phytoplankton or harmful algae blooms (Cai et al., 2016). Such blooms significantly lower the oxygen levels and consequently result in the spreading of coastal hypoxic zone, endangering coastal and

marine ecosystems (Cai et al., 2016). Hence, it is crucial to investigate the characteristics and controlling mechanisms of marine heatwaves in the ECSs.

The ECSs have experienced warming trend during the recent four decades (Yeh and Kim 2010; Oey et al., 2013; Cai et al., 2017). Previous studies mainly discussed the long-term ocean warming: both Yeh and Kim (2010) and Oey et al. (2013) studied the decadal warming and its drivers during winter whereas Cai et al. (2017) investigated the inter-decadal warming during both winter and summer. However, event specific studies about marine heatwaves in ECSs are rare. In August 2016, record-breaking monthly mean sea surface temperature (SST) emerged in the ECS, as indicated in the NOAA OISST (National Oceanic and Atmospheric Administration's Optimum Interpolation Sea Surface Temperature) data (Tan and Cai, 2018). Strikingly, the NOAA OISST data show that SST anomalies in August 2017 were even stronger and covered wider areas in the ECSs, followed with another warm summer in 2018 (Figure 2). Three successive warm summers, including two record-breaking ones, were unprecedented in the past four decades, which motivates us to examine the anomalous atmospheric and oceanic conditions responsible for those MHWs.

The current system during summers in the ECSs mainly consists of cyclonic (anticlockwise) circulation over the SYS (Beardsley et al., 1992; Yanagi and Takahashi, 1993; Xia et al., 2006), and the Taiwan–Tsushima warm currents (Isobe, 2004 and 2008) and the Kuroshio Current (Wang and Oey, 2014; Yang et al., 2018) in the ECS. There are also the northward Chinese coastal currents (Naimie et al., 2001). NCEP (National Center for Environmental Prediction) or ECMWF (European Centre for Medium-Range Weather Forecasts) reanalysis data set are useful in exploring the warming trend of ECSs on long time scales (Yeh and Kim, 2010; Oey et al., 2013; Park et al., 2015; Cai et al., 2017), but they lack spatial resolution to capture the complicated current system in the ECSs. What is more, tides are of significant importance to the hydrodynamics in ECSs (e.g. Naimie et al., 2001; Xia et al., 2006; Lozovatsky et al., 2007a, b;) which are not considered in the NCEP and ECWMF

products. Therefore, ocean processes with respect to warm summers during 2016-2018 may not be well quantified by these reanalysis products (Tan and Cai, 2018). A well-validated regional model with high spatial resolution would be crucial to reproduce the anomalous warming patterns, thereby quantifying the contribution of responsible processes with better accuracy (Frölicher et al., 2018). Improved modelling of MHWs can in turn allow the development of MHW forecasting system in the ECSs region which to help critical fisheries and aquaculture industries to better plan their annual activities.

Major processes controlling summer surface temperature variations in the ECSs include heat advection by the ocean currents (Tan and Cai, 2018), air-sea heat flux, mainly controlled by the East Asian Summer Monsoon (Oey et al., 2013; Cai et al., 2017) and the Western Pacific Subtropical High (Matsumura et al., 2015; Tan and Cai, 2018), and local vertical mixing (Xie et al., 2002). Different MHW events may involve different combination of the mechanisms. The aim of this study is to use the regional ocean model to examine the atmospheric and oceanic mechanisms responsible for three successive warm summers (June, July and August; JJA hereafter) in the ECSs.

The rest of the paper is organized as follows. The data, numerical modelling and analysis method are introduced in section 2. Section 3 presents the details of temperature budgets and investigations on major drivers. Section 4 summarizes the main findings.

2. Data and Methods

2.1 SST data

The SST data used in this study are NOAA OISST version 2 (Reynolds et al., 2007), which is a daily and 0.25˚×0.25˚ gridded product of Advanced Very High Resolution Radiometer (AVHRR) satellite data provided by the NOAA/OAR/ESRL PSD, Boulder, Colorado, USA, accessed from their Web site at

https://www.esrl.noaa.gov/psd/. Satellite bias was corrected with respect to in-situ data from ships and buoys (Reynolds et al., 2007). Data are available from September 1, 1981 to present.

2.2 Atmospheric data

To investigate the role and contribution of atmospheric and radiative forcing to the three consecutive warm summers, we used data from the NCEP Climate Forecast System Reanalysis (CFSR), version 2 product (Saha et al., 2013). CFSRv2 is the reanalysis product of the fully coupled atmosphere-ocean-land model Climate Forecast System version 2 (CFSv2) implemented in March 2011. It uses the NCEP Global Forecast System (GFS) as its atmospheric model and the Modular Ocean Model, version 3 (MOM3), from the Geophysical Fluid Dynamics Laboratory (GFDL). CFSv2 includes two data assimilation systems namely the NCEP-Department of Energy (DOE) Global Reanalysis 2 (Kanamitsu et al., 2002) and the Global Ocean Data Assimilation System (GODAS; Behringer, 2007). Data used in this study included hourly 10m winds, surface air temperature, air pressure and relative humidity, downward longwave and shortwave radiations at the surface, and precipitation rates and geopotential height at 850 hPa and 500 hPa on a 0.2×0.2 degrees spatial grid. Monthly outputs of the first version of CFSR (Saha et al., 2010a, b) at a resolution of 0.312×0.312 degrees were used to compare recent atmospheric conditions with the long-term climatology.

2.3 Numerical modelling

2.3.1 Model setup

The Unstructured-grid Finite Volume Community Ocean Model (FVCOM; Chen et al., 2003) was adopted to simulate the ocean dynamics in this region. The model mesh and configuration used in study were the same as that of Ding et al. (2018) and Ding et al. (2019), which investigated coastally trapped waves and ocean current

fluctuations under storms in the ECSs. In this study, the model is named as FVCOM-ECSs.

The FVCOM-ECSs mesh consists of 70,479 nodes and 136,612 elements, covering the Bohai Sea (BS), the North Yellow Sea (NYS), the SYS and the ECS (Figure 1b). The horizontal resolution increases gradually from 20 km near the open boundary toward around 1 km along the coastal regions. In the vertical direction, 30 sigma layers are evenly distributed in the terrain-following coordinate. The bathymetry data used in this model are primarily obtained from DBDB5 (U.S. Naval Oceanographic Office 1983), combined with topography data from the China coastal sea chart database to gain higher resolution along the Chinese coast. The wet and dry treatment is embedded in the model. The vertical eddy viscosity is calculated using Mellor and Yamada (1982) turbulent closure model and the horizontal diffusion coefficient is determined by Smagorinsky eddy parameterization method (Smagorinsky 1963).

In FVCOM-ECSs, the open boundary forcing such as sub-tidal sea surface heights, currents, temperature and salinity on daily time scale were derived from the global model of Estimating the Circulation and Climate of the Ocean Phase II (ECCO2, Menemenlis et al. 2008). Hourly tidal levels and barotropic tidal currents were obtained from TPXO 7.2 based on nine tidal constituents (M_2, S_2, N_2, K_1, O_1, Q_1, M_4, MS_4, MN_4). The global ECCO2 model outputs were also used for the initial temperature and salinity fields of the FVCOM-ECSs. The ECCO2 data can be derived from the Asia–Pacific Data-Research Center of the IPRC (APDRC, http://apdrc.soest.hawaii.edu/index.php). Surface forcing data acquired from CFSRv2 were hourly 10m winds, surface air temperature and relative humidity, downward longwave and shortwave radiations at the surface, and precipitation rates. Latent heat flux and sensible heat flux were calculated using bulk formulation (Fairall et al., 1996; Subroutine COARE26Z in FVCOM 3.2.2). Two major rivers (Changjiang River and Yellow River) were considered: the temperature was specified referring to daily Multi-sensor Ultra-high Resolution (MUR) SST; the salinity was set to be constant at

5 psu in the model; monthly-averaged freshwater discharge data were provided by the Information Center of Water Resources, Bureau of Hydrology, Ministry of Water Resources of P. R. China.

The model run was carried out from January 01, 2012 to August 31, 2018. The first year was regarded as spin up and model outputs from January 01, 2013 were analyzed.

2.3.2 Model validation

The FVCOM-ECSs has been extensively validated in terms of barotropic tides, sub-tidal sea levels and currents, temperature, salinity, and surface waves (Ding et al., 2011; Ding et al., 2018; Gao et al., 2018; Ding et al., 2019). Since the FVCOM-ECSs is able to capture the key hydrodynamics features of the ECSs, in this study we focus on the evaluation of the SST variability between the model results and the NOAA OISST product.

Compared with satellite observations, the FVCOM-ECSs SST has a mean bias around 0.2°C, with the RMSE smaller than 0.8°C in most parts of the study area (Figure 3a, b). The correlation coefficients between the satellite and FVCOM-ECSs SST are higher than 0.95 in most of the ECSs (Figure 3c). The mean bias and RMSE are large in the Kuroshio Current (KC) region – note that the depth there is deeper than 2000 m and 30 uniform sigma layers may not be sufficient to capture the SST variability. Nevertheless, the FVCOM-ECSs reproduced the SST anomalies in the satellite observations during 2013-2018 (Figure 4).

Figure 4 shows that the FVCOM-ECSs successfully captured the position and strength of SST anomalies from 2013 to 2018: one warm summer in 2013, two neutral summers in 2014 (slightly cold) and 2015, and three consecutive warm summers from 2016 to 2018. Anomalous warm waters were primarily found in the SYS and the north part of the ECS. In July 2017, positive SST anomalies were the highest and covered the largest area. Three-year (2013 to 2015) averaged model results were used

as the normal-year average or baseline reference in this study. The 2013 to 2015 averaged SST show a quite similar pattern to the long-term (1982 to 2016) averaged SST (support information Figure S1), so it is reasonable to use 2013 to 2015 model results as the baseline reference.

The statistical comparison of daily SST during summers (JJA) from 2013 to 2018 between the model and the satellite data (Figure 5) confirmed that the FVCOM-ECSs could reproduce daily SST variations in most parts of the study domain, except in the near shore areas and in the KC region. Two boxes (Boxes SYS and NECS), with strong SST anomalies and good model performances (Figures 3-5), are used for heat balance analysis. Box SYS covers the China shelf and the center trough of the SYS (121-125.9°E, 33.65-37.4°N) and Box NECS is the central shelf of the ECS, located in the north part of ECS adjacent to the SYS (123-126°E, 30-33.65°N). The model accurately reproduced the observed normal-year average (2013 to 2015 mean) SST evolution in Boxes SYS and NECS, as shown in a 11-day running mean (Figures 6a, b). The SST anomalies relative to normal-year average are also compared well with observations for both Boxes in 2016, 2017 and 2018 (Figure 6c, d). For Box SYS, the modelled SST anomalies generally agreed well with satellite data during JJA in 2016 and 2018, whereas the peak SST anomalies in July 2017 were underestimated by the model. For Box NECS, in 2017 and 2018, the model simulated the increases of SST anomalies from June 1st to the peak values, however, it underestimated the decay of the SST anomalies after the peak; SST anomalies in 2016 experienced two peaks and the model slightly underestimated the first peak but well captured the second peak. Direct comparison of daily SST in JJA during 2016-2018 between the model results and satellite data is provided in the support information (Figure S2). Overall, the model was able to reproduce the normal-year averaged SST and increasing trends of SST anomalies from the beginning of June to the summer peak values for both Boxes SYS and NECS in 2016-2018.

2.4 Marine Heatwave Definition and Metrics

The Hobday et al (2016) definition was used to characterize the warming events in summers during 2016-2018. According to Hobday et al (2016), a MHW is defined as an anomalously warm, discrete, and prolonged event, which can be quantitatively described as periods of time when daily temperatures are above a particular threshold for at least five days. The threshold is calculated as the 90th percentile of daily temperature variability across a >30-year period, within an 11-day window centered on a specific day of the year. This seasonally varying threshold allows for events to occur at any time of the year. Threshold and climatological values were derived using the NOAA OISST. Here, we chose a fixed baseline climatological period following Hobday et al. (2016), as a baseline of at least 30 years is necessary to capture most of the variability. Due to the limited length of observation timeseries, it was not possible to adopt a moving baseline, as advocated for climate change studies (Jacox, 2019). Consistent with atmospheric heatwave definition, two successive events with a gap of 2 days or less are considered as a single continuous event.

A set of metrics are used to quantify a MHW once it is identified. Three metrics are used in the study: the duration (days between the start and end dates), the maximum intensity (maximum SST anomalies during a single event) and the cumulated intensity (sum of daily intensity anomalies measured in °C days).

2.5 Upper ocean temperature budget

The upper ocean temperature budget is calculated with volume-averaged temperature tendency equation from sea surface to a fixed depth h, and within a surface area A.

$$\underbrace{\frac{\partial \langle T \rangle}{\partial t}}_{RATE_v} = \underbrace{-\langle u_H \cdot \nabla T \rangle}_{Adv_H} \underbrace{-\left\langle w \frac{\partial T}{\partial z} \right\rangle}_{Adv_V} + \underbrace{\frac{1}{\rho C_P A} \int^A \frac{Q}{h} \mathrm{d}A}_{Q_v} \underbrace{-\frac{1}{Ah} \int^A \left(\kappa_v \frac{\partial T}{\partial z} \right)_{-h} \mathrm{d}A}_{V_{mix}} \underbrace{-\langle \nabla \cdot (\kappa_h \nabla T) \rangle}_{Residuals} \quad (1)$$

Where T is the volume-averaged temperature; t is the time; $\langle\ \rangle = \frac{1}{hA} \int^A \int_{-h}^{0} \mathrm{d}z\mathrm{d}A$ represents volume average; u_H is the horizontal current vector;∇ is the horizontal gradient operator; w is the vertical current; Q=Q_{sw}(0)- Q_{sw}(h)+ Q_{lw}+Q_{lh}+Q_{sh} is the net

heat flux which is the summation of shortwave radiation absorbed in the top h m $Q_{sw}(0)$- $Q_{sw}(h)$, longwave radiation Q_{lw} , latent heat flux Q_{lh} and sensible heat flux Q_{sh}. $Q_{sw}(z)$ is the shortwave radiation penetrated at depth z (see details in Paulson and Simpson, 1977). κ_v and κ_h are the horizontal and vertical eddy diffusivities. The residuals contain the horizontal diffusion terms. The temporal-rate of volume-averaged temperature change $RATE_V$ is decomposed into following terms: horizontal advection Adv_H, vertical advection Adv_V, net heat flux Q_v, vertical mixing V_{mix} and residuals. Those diagnostic terms are calculated online for every time step of the FVCOM-ECSs.

The total contribution of advection (Adv_H+Adv_V) were diagnostically output from the model but the directions were only distinguished into inward or outward the "tracer volume element" (see the finite volume method in Chen et al., 2013).Therefore, the contributions from five different boundaries of Boxes SYS and NECS were calculated based on daily-averaged temperature and currents outputted by the model.

$$Adv_H + Adv_v = \underbrace{\frac{1}{V}\iint_{Sb} v(T-\langle T\rangle)dxdz}_{South} \underbrace{-\frac{1}{V}\iint_{Nb} v(T-\langle T\rangle)dxdz}_{North} + \underbrace{\frac{1}{V}\iint_{Wb} u(T-\langle T\rangle)dydz}_{West} \underbrace{-\frac{1}{V}\iint_{Eb} u(T-\langle T\rangle)dydz}_{East}$$

$$\underbrace{+\frac{1}{V}\iint_{A} w_{-h}(T_{-h}-\langle T\rangle)dxdy}_{Vertical} + Residuals \qquad (2)$$

Sb, Nb, Wb, Eb represent the south, north, west and east boundaries of a box respectively. *V* is the volume of a Box. The residuals in Eq (2) may come from the interpolation errors from unstructured grids into the regular boundaries.

Advection-induced temperature anomalies are associated to the anomalies of currents and temperature. Contributions of advection at any boundary can be further decomposed into (Using the south boundary as an example):

$$\underbrace{\frac{1}{V}\iint_{sb} v(T-\langle T\rangle)dxdz}_{South} =$$

$$\underbrace{\frac{1}{V}\iint_{Sb} \bar{v}\left(\overline{T}-\langle\overline{T}\rangle\right)dxdz}_{Normal-year\ avergae} + \underbrace{\frac{1}{V}\iint_{Sb} v'\left(\overline{T}-\langle\overline{T}\rangle\right)dxdz}_{Current\ anomaly} + \underbrace{\frac{1}{V}\iint_{Sb} \bar{v}\left(T^{'}-\langle T^{'}\rangle\right)dxdz}_{Temperature\ anomaly} +$$

$$\underbrace{\frac{1}{V}\iint_{Sb} v'\left(T^{'}-\langle T^{'}\rangle\right)dxdz}_{Eddy} \quad (3)$$

Over bar represents the normal-year average and prime represents the anomaly in individual year.

3. Results

3.1 Characteristics of three successive warm summers from 2016 to 2018

Figure 2 summarizes the MHW characteristics for the ECSs, derived from the SST observations. in the large ECSs Box, both 2016 and 2017 summers had well-defined, unprecedented MHW events (Figures 2b-d), in terms of maximum intensity (3°C) in 2016 and in terms of duration and cumulated intensity (44 days and 85.5°C days) in 2017. There was a strong summer MHW in 1994, nearing maximum values of duration, intensity and cumulated intensity, which might be associated with the Asian heat wave during that summer (Park, and Schubert, 1994). MHWs during the 2018 summer were weaker than the two previous years, despite occurring at several short periods. Despite high values of MHW maximum intensity (2°C), 2018 summer events lasted less than 10 days, resulting in a weak cumulative intensity (Figures 2b-d). Overall, more frequent summer MHW events occurred after 1997 (Figures 2b-d). The decadal increase in MHW frequency is likely due to the long-term warming trend observed since the beginning of the 20th century (Oliver, 2019; Oliver et al., 2018), although there appears to be a halt in the warming trend in the ECSs box since the late 1990s (Figure 2a).

In both the SYS and the NECS boxes, the main 2016 summer MHW started in early August, with maximum SST anomalies peaked a few days earlier in the SYS than in the NECS, both reaching ~4°C. While temperatures were above the climatological

average in the SYS at the start of the 2016 summer, there was a progressive warming of SSTs in the NECS, from a relatively cool state at the start of summer (Figures 2e and 2h). In 2017, SSTs were above the MHW threshold at the start of the summer for both boxes and remained above the threshold during most of the summer (Figures 2f and 2i). The main event occurred in early June and late June for the SYS and NECS and lasted until mid-August. In the 2018 summer, temperatures in the NECS only briefly crossed the MHW threshold, not persistent enough to be classified as a MHW (Figure 2j). However, a strong MHW occurred in the SYS, starting late July and lasting for about 20 days (Figure 2g), with a maximum intensity of about 3°C.

3.2 Temperature budget

SST anomalies during 2016-2018 generally emerged in June and peaked in July or August, so that we calculated the daily upper ocean temperature budget during the JJA period. In both Boxes SYS and NECS (Figures S3, S4), anomalous warmings were most significant in the top 20 m in the summers of 2016 to 2018. In 2018, anomalous warming in Box SYS extended to the subsurface layer toward the end of summer. Subsurface warming was also present in Box NECS during the first half of summer 2017. In this study, we focused the anomalous warming in the top 20 m because: 1) the anomalous warming were most significant in the top 20 m for both boxes; 3) 20 m reflects the summer mixed layer depth; and 3) the model SST agreed well with satellite data. In areas where water depth is shallower than 20 m, the integration is between sea surface and sea floor. It is noted that water depths are deeper than 20 m in most areas in Boxes SYS and NECS.

Box SYS

During the normal year, the top 20 m temperature in the SYS box warmed up from about 16˚C at June 1st of each year to about 23˚C toward the end of summer, with a 15˚C warming contribution from the net air-sea heat flux, countered by a ~7˚C cooling from vertical mixing (Figure 7a).

Positive temperature anomalies in the SYS during summer 2016-2018 were mainly caused by net air-sea heat flux and advection anomalies (Figures 7b-d): In 2016, the anomalous net heat flux dominated the temperature variability; in 2017, net heat flux dominated in June and July, but contribution of advection anomalies became important during the first half of August; in 2018, both the net heat flux and advection anomalies drove the rise of the temperature anomalies, with the advection effects more important toward to the second half of August. The initial temperature anomaly of 0.5˚C on 1 June 2017 also contributed the warm event during that summer.

Within the net heat flux, shortwave radiation dominated not only the temperature variation during a normal year but also the temperature anomalies during the three anomalous summers (Figures 8a-d). Anomalous shortwave radiation warmed the SST during around whole JJA in 2017 and during the latter half of JJA in 2016 and 2018. The other heat flux terms had weak or slightly cooling effects.

Anomalous heat advection across the south, west and vertical (bottom) boundaries contributed to the summer warming in Box SYS in 2016 and 2017 (Figure 8f, g). The effects of advection were much more prominent in 2018: vertical advection anomalies and horizontal advection anomalies at the south boundary caused significant anomalous warming in the second half of the 2018 summer (Figure 8h).

We further examined the causes of the peak temperature anomalies in Box SYS for the three summers (Table S1). Shortwave radiation was the most important factor leading to peak anomalous temperature anomalies, with contributions of 1.51°C, 0.8°C and 1.67°C during the summers in 2016, 2017 and 2018, respectively. In 2018, the contribution of advection to peak temperature anomaly reached 1.55 °C, with 1.04 °C and 0.72 °C contributed across the vertical and south boundaries, respectively. Regression analysis shows that daily anomalous temperature changes were significantly correlated to both advection and shortwave radiation anomalies during JJA in Box SYS (Figure S5).

Box NECS

Whereas net heat flux and advection anomalies played critical roles in anomalous temperature changes in Box NECS, the role of vertical mixing also became important (Figures 9b-d). Shortwave radiation anomalies still played a leading role among all the heat flux terms to warm the upper ocean (Figures 10b-d). In 2016, shortwave radiation became significant from mid-August while reduction of latent heat loss provided additional warming effects (Figure 10b), as a result of reduced wind speeds compared to normal-year averages (support information Figure S6). In 2017, wind speeds were reduced but the specific humidity were also reduced (support information Figure S7), thus latent heat flux showed an overall cooling effect. The shortwave radiation anomalies were most significant in 2018, dominating over the other flux terms (Figure 10d).

Advection was important during summers in 2017 and 2018 (Figures 10g, h), contributing 0.84 °C and 1.36°C to the peak temperature anomalies respectively (Table S2). In 2016, temperature anomalies induced by advection was generally negative (Figure 10f). Whereas effects of advection at various boundaries were quite different among three summers, horizontal advection across the south boundary consistently contributed to warming events (Figures 10f-h).

Reduction of vertical mixing was crucial to the summer warming in Box NECS in 2016 and 2017 (Figures 9b, c). Vertical mixing contributed to 0.87 °C and 1.12 °C of the maximum surface temperature anomalies in 2016 and 2017, respectively, and the anomalies of daily temperature changes had significant correlations with that caused by vertical mixing variability (Figure S8).

In the next three subsections, we discuss the drivers of the anomalous increase of shortwave radiation, the ocean current anomalies, and the reduction of upper ocean vertical mixing in Box NECS.

3.3 Shortwave radiation

Positive anomalies of shortwave radiations occurred during all three summers in 2016-2018, relative to 2013-2015 average, in a zonal band between 30-35°N extending from eastern China to Japan (Figures 11a-c). The magnitude and pattern of the positive anomalies of shortwave radiation remained the same when using a longer term climatology (Figure S9). The main weather system controlling cloud formation and rainfall in the ECS during summer is the East Asian Summer Monsoon (EASM; Ding and Chan (2005). The onset of the EASM expresses itself as enhanced rainfall in the South Asia region at the end of May, extending abruptly to the Yangtze River basin in East China in early June. Monsoonal rain then moves northeastward towards the ECSs and the Korean Peninsula, expressed as a frontal cloud zone called the Meiyu-Baiu front/rainband (Ninomiya, 2004).

The mechanisms of the EASM variability are still not fully understood due to the complexity of the system. The primary external forcing for the onset of the EASM are believed to be the Pacific and Indian Ocean SST variations, as well as the snow cover on the Tibetan Plateau (Ding and Chan, 2005; Zhou et al., 2009). However, internal variability of the regional atmospheric circulation determines the position and intensity of the cloud front. Pressure and wind anomalies at 850hPa showed a westward shift of the Western Pacific Subtropical High (WPSH) in 2016 and 2017 and a northward displacement of the WPSH in 2018 (Figures 11g-i). Pressure and wind climatologies at 850hPa and 500hPa can be found in the Supplementary file (Figure S10). The intensity and location of the WPSH is well correlated with the Meyiu-Baiu front activity and can represent leading EOF modes of the EASM (Huang et al., 2018; Oppenheim et al., 1999; Wang et al., 2013). The associated changes in low level circulation likely modified the EASM intensity via a decrease of moisture transport and/or horizontal thermal gradient (Lee et al., 2013; Ding and Chan, 2005), or shifted the location of the Meiyu-Baiu front (Gao et al., 2016).

The mid-level East Asian Westerly Jet (EAWJ) was also found to have a profound impact on the EASM. Several studies showed that the position of the EAWJ impacted

the amount of precipitation in the Yangtze River basin (Du et al., 2009; Xuan et al., 2011). Recently, the EAWJ intensity was found to be positively correlated with precipitation in the Yangtze River basin (Wang and Zuo, 2016). Anomalies of winds at 500hPa showed that the EAWJ was weaker in 2017 and shifted north in 2016 and 2018 (Figures 11d-f), helping to weaken the frontal system and increase shortwave radiation irradiance.

Despite the roles that both the WPSH and the EAWJ likely played in increasing shortwave irradiance during the recent summers, our understanding of the complex EASM system remains limited. Further research is needed to explain the recent increases of summer shortwave radiations over the ECSs.

3.4 Ocean currents

Since the contribution of advection to the anomalous warming is determined by the variability of ocean currents and temperature. The effects of current anomalies played a more important role than those due to temperature anomalies for both Boxes (Figures S12, S13). Thus, in this section, we further examine the effects of current anomalies during the three warm summers.

As shown in Figure S11a (support information), the FVCOM-ECSs has successfully reproduced the cyclonic circulation (jet like southward currents in the west portion and northward currents in the east portion of the central trough) in the SYS (Beardsley et al., 1992; Yanagi and Takahashi, 1993; Xia et al., 2006), northward currents along the Chinese coast (Naimie et al., 2001), and the Taiwan–Tsushima warm current system (Isobe, 2004 and 2008). Current anomalies averaged during JJA were much prominent in 2018 than those in 2016 and 2017.

For better illustration, currents anomalies during the periods from June 1st to the day when peak temperature anomalies occurred during JJA in each year (2016 to 2018) are plotted in Figures 12a-c (Box SYS) and 13a-c (Box NECS). The anomalies of wind stress and stress curls averaged during corresponding periods are shown in

Figures 12g-i (Box SYS) and 13g-i (Box NECS). Normal-year averages (2013-2015) and anomalies (2016-2018) of wind stress and wind stress curls averaged during JJA can be seen in Figure S14. To investigate the local wind effects on the current system, we conducted a model run (Experiment 1) in which we replaced the wind forcing in JJA 2016 to 2018 with the normal-year averaged wind forcing (2013 to 2015 average) and then analyzed the current anomalies averaged during corresponding periods (Figures 12d-f and 13d-f).

Box SYS

In 2017, anomalous downwelling covered more than half of Box SYS and northward current anomalies were found in the west part of south boundary (Figure 12b), where temperatures were higher than the box average, both contributing to the maximum temperature anomalies of Box SYS. In 2018, anticylonic current anomalies and downwelling dominated the whole Box SYS (Figure 12c). Northward current anomalies were significant in the south boundary as well. Therefore, advection in the south and vertical boundaries contributed to more than half of the maximum temperature anomalies of Box SYS in 2018. The current anomalies were absent in experiment 1 (Figures 12d-f), confirming that current anomalies in Box SYS were due to the regional winds anomalies.

Box NECS

Northward currents along the Chinese coast (31 to 35°N; west to 124°E) were strengthened (Figures 13b, c) by the anomalous northward winds (Figures 13h, i) in both 2017 and 2018, which transported more heat into Box NECS from the south or west boundary. The anomalous wind stress curl also drove downwelling anomalies (Figure 13c), contributing to the anomalous warming in 2018.

In 2017, strengthen northeastward currents were found between 125 and 127°E in the east part of Box NECS, which transported more heat out of Box NECS at the east boundary (Figure 13b). However, current anomalies were southwestward between 125 and 127°E in 2018 (Figure 13c), which was not sensitive to the local wind

anomalies. Thus, currents anomalies between 125 and 127°E were likely due to inter-annual variations of the Tsushima Warm Currents (TsWC). The TsWC on the shelf of the ECS originates from Taiwan Warm Current (TWC) and intrusions from the Kuroshio Current (KC) (Fan, 1982; Guan and Fang, 2006; Guo et a., 2006; Ma et al., 2010). The TsWC variability is primarily forced by the open ocean processes through the KC rather than TWC (Yang, 2007; Zheng et al., 2009; Ma et al., 2010).

3.5 Vertical mixing

Figures 14a, b shows that anomalies of daily temperature changes in Box NECS during three warm summers was remarkably well correlated with vertical eddy viscosity anomalies, other than vertical temperature gradient anomalies. From the model, vertical eddy viscosities in the upper 20 m averaged during JJA were reduced in 2016 and 2017 and enhanced in 2018 (Figure 14c), thus, the vertical mixing anomalies contributed to the anomalous warming in 2016 and 2017 but not in 2018. Surface wind plays a major role in driving the vertical mixing in the upper layer of the ECSs (Park and Chu 2007; Xuan et al., 2012). Note the magnitudes of wind speed in Box NECS were reduced in 2016 and 2017 but increased in 2018 (Figures S6d-g). Temperature anomalies in Box NECS had a sharp decrease near the end of August in 2018 (Figure 9d), which was probably related to the vertical mixing associated with the passage of Typhoon Soulik.

When model was driven by the normal-year averaged wind speeds (experiment 1), the vertical eddy viscosities had negligible differences among three warm summers (Figure 14d). This further confirms the role of wind speed anomalies on the anomalous vertical mixing. It should be mentioned that magnitudes of winds speeds in experiment 1 were smaller than the normal-year averaged magnitudes of wind speeds (Figures S15), thus the vertical eddy viscosities (2016 to 2018) in experiment 1 were smaller than the normal year averages in the control experiment (Figure 14d).

4. Summary and conclusion

The ECSs (East China Sea and the South Yellow Sea) experienced unprecedented MHW events during three consecutive summers from 2016 to 2018. Using the outputs from a well-validated hydrodynamics model with high spatial resolution, we investigated the roles of oceanic processes and air-sea heat flux in the extreme warming of top 20m in two regions in the ECSs. Temperature budget for the top 20 m in Boxes SYS and NECS illustrates that these warm summers were associated with variations of shortwave radiation, advection and vertical mixing. Positive shortwave radiation anomalies during JJA from 2016 to 2018 are associated with the reduction of cloud cover in the Meiyu-Baiu front/rain region, and both the intensity and position of the WPSH and EAWJ likely contributed to the weakening and/or northward shift of Meiyu-Baiu front/rainband. Northward current anomalies transported more heat into Boxes SYS and NECS at from the south boundary during the three summers. Downwelling anomalies dominated Box SYS in 2018, which significantly enhanced the warming of the surface layer. Over whole Box SYS and west part of Box NECS, currents anomalies in both horizontal and vertical directions were forced by the anomalous wind stress and stress curls. In addition, reductions in the magnitudes of wind speeds over Box NECS weakened the local vertical mixing and significantly intensified the anomalous warming in 2016 and 2017. This research highlights that a high-resolution ocean modelling is necessary to understand the local and remote processes in the driving the marine heatwaves in the coastal regions. The identification of roles of the East Asian Monsoon system in the MHW developement in the ECSs may help MHWs dynamics in other coastal regions at middle latitudes where the monsoon system is dominant during the summer season.

Acknowledgement

This work was supported by the National Natural Science Foundation of Shandong Province (No. 41406097) and CAS-CSIRO funding. This study was also supported by the Major Research Grant from Both the National Natural Science Foundation of China (NSFC) and the Provincial Natural Science Foundation of Shandong (NSFSD)

(Ref No: U1806227). Dezhou Yang was supported by the National Natural Science Foundation of China (NSFC) (41576023, 41876019). Yang Ding was supported by the National Natural Science Foundation of China (No. 41430963). The FVCOM-ECSs model data is available from the Marine Science Data Center of Institute of Oceanology, Chinese Academy of Sciences (http://159.226.158.89:38817/thredds/catalog/Ggd/catalog.html).

Reference

Beardsley, R. C., R. Limeburner, K. Kim, and J. Candela (1992), Lagrangian flow observations in the East China, Yellow and Japan Seas, La Mer, 30, 297–314.

Behringer, D. (2007), The Global Ocean Data Assimilation System (GODAS) at NCEP, 87th AMS Annual Meeting.

Benthuysen, J., M. Feng, and L. Zhong (2014), Spatial patterns of warming off Western Australia during the 2011 Ningaloo Nin˜o: quantifying impacts of remote and local forcing, Continental Shelf Research, 91, 232–246.

Benthuysen, J. A., E. C. J. Oliver, M. Feng, and A. G. Marshall (2018), Extreme marine warming across tropical Australia during austral summer 2015-16, Journal of Geophysical Research: Oceans, 123, 1301–1326.

Bond, N. A., M. F. Cronin, H. Freeland, and N. Mantua (2015), Causes and impacts of the 2014 warm anomaly in the NE Pacific, Geophysical Research Letters, 42, 3414–3420.

Cai, R., H. Tan, and Q. Qi (2016), Impacts of and adaptation to inter-decadal marine climate change in coastal China seas, International Journal of Climatology, 36(11), 3770–3780.

Cai, R., H. Tan, and H. Kontoyiannis (2017), Robust surface warming in offshore China seas and its relationship to the east Asian monsoon wind field and ocean forcing on interdecadal time scales, Journal of Climate, 30(22), 8987–9005.

584 Cai W. J, X. Hu, W. J. Huang, M. C. Murrell, J. C. Lehrter, S. E. Lohrenz, W. C.
585 Chou, W. D. Zhai, J. T. Hollibaugh, Y. C. Wang, P. Z. Zhao, X. Guo, K. Gundersen
586 K, M. H. Dai, and G. C. Gong (2011), Acidification of subsurface coastal waters
587 enhanced by eutrophication, Nature Geoscience, 4(11), 766–770.

588 Caputi, N., M. Kangas, A. Denham, M. Feng, A. Pearce, Y. Hetzel, and A.
589 Chandrapavan (2016), Management adaptation of invertebrate fisheries to an extreme
590 marine heatwave event at a global warming hot spot, Ecology and Evolution, 6, 3583–
591 3593.

592 Chen, C., H. Liu, and R. C. Beardsley (2003), An unstructured grid, finite volume,
593 three-dimensional, primitive equations ocean model: Application to coastal ocean and
594 estuaries, Journal of Atmospheric & Oceanic Technology, 20, 159–186,
595 doi.org/10.1175/1520-0426(2003)020,0159:AUGFVT.2.0.CO;2.

596 Chen C., R.C. Beardsley , G. Cowles, J. Qi, Z. Lai, G. Gao, D. Stuebe, Q. Xu, P. Xue,
597 J. Ge, S. Hu, R. Ji, R. Tian, H. Huang, L. Wu,H. Lin, Y. Sun and L. Zhao (2013), An
598 Unstructured Grid, Finite-Volume Community Ocean Model FVCOM User Manual,
599 SMAST/UMASSD-13-0701.
600 Chen, K., G. G. Gawarkiewicz, S. J. Lentz, and J. M. Bane (2014), Diagnosing the
601 warming of the Northeastern US Coastal Ocean in 2012: a linkage between the
602 atmospheric jet stream variability and ocean response, Journal of Geophysical
603 Research: Oceans, 119, 218–227.

604 Di Lorenzo, E. and N. Mantua (2016), Multi-year persistence of the 2014/15 North
605 Pacific marine heatwave, Nature Climate Change, 6, 1042–1047.

606 Ding, Y. and J. C. L. Chan (2005), The East Asian summer monsoon: and overview,
607 Meteorology & Atmospheric physics, 89:117-142.

608 Ding, Y., H. M. Yu, X. W. Bao, L. Kuang, C. X. Wang, and W. J. Wang (2011),
609 Numerical study of the barotropic responses to a rapidly moving typhoon in the East
610 China Sea, Ocean Dynamics, 61, 1237~1259, doi:10.1007/s10236-011-0436-1.

611 Ding, Y., X. Bao, Z. Yao, D. Song, J. Song, J. Gao, and J. Li (2018), Effect of
612 coastal-trapped waves on the synoptic variations of the Yellow Sea Warm Current
613 during winter, Continental Shelf Research, 167, 14-31.

614 Ding, Y., X. Bao, Z. Yao, C. Bi, K. Wan, M. Bao, Z. J., J. Song, and J. Gao (2019),
615 Observational and model studies of synoptic current fluctuations in the Bohai Strait
616 on the Chinese continental shelf, Ocean Dynamics, doi:10.1007/s10236-019-01247-5.

617 Du, Y., Y. Zhang, and Z. Xie (2009), Impacts of the Zonal Position of the East Asian
618 Westerly Jet Core on Precipitation Distribution During Meiyu of China, Acta
619 Meteorologica Sinica.

620 Fairall, C. W., E. F. Bradley, D. P. Rogers, J. B. Edson, and G. S. Young (1996), Bulk
621 parameterization of air-sea fluxes for Tropical ocean-global atmosphere coupled–
622 ocean atmosphere response experiment, Journal of Geophysical Research, 101(C2),
623 3747–3764, doi:10.1029/95JC03205.

624 Fan, K. L. (1982): A study of water masses in Taiwan Strait. Acta Oceanographica
625 Taiwanica, 13, 140–153.

626 Frölicher, T. L., E. M Fischer, and N. Gruber (2018), Marine heatwaves under global
627 warming. Nature 560, 360–364, doi:10.1038/s41586-018-0383-9.

628 Gao, G. D., X. H. Wang, D. H. Song, X.W. Bao, B. S. Yin, D. Z. Yang, and Y. Ding
629 (2018), Effects of wave-current interactions on suspended-sediment dynamics during
630 strong wave events in JiaozhouBay, Qingdao China, Journal of Physical
631 Oceanography, 48, 1053-1078, doi: 10.1175/JPO-D-17-0259.1.

632 Gao, Q., Y. Sun, and Q. You (2016), The northward shift of Meiyu rain belt and its
633 possible association with rainfall intensity changes and the Pacific-Japan pattern,
634 Dynamics of Atmospheres and Oceans, 76, 52–62,
635 doi.org/10.1016/j.dynatmoce.2016.08.005.

636 Guan, B. X. and G. H. Fang (2006), Winter counter-wind currents off the southeastern
637 China coast: A review, Journal of Oceanography, 62(1), 1–24.

638 Hobday, A. J., L. V. Alexander, S. E. Perkins, D. A. Smale, S. C. Straub, E. C. Oliver,
639 E. C.,… T. Wernberg (2016), A hierarchical approach to defining marine heatwaves,
640 Progress in Oceanography, 141, 227–238, doi.org/10.1016/j.pocean.2015.12.014

641 Hu, M. N., and C. F. Zhao (2008), Upwelling in Zhejiang coastal areas during
642 summer detected by satellite observations, Journal of Remote Sensing, 12(2), 297–
643 304.

644 Huang, Y., B. Wang, X. Li, and H. Wang (2018), Changes in the influence of the
645 western Pacific subtropical high on Asian summer monsoon rainfall in the late 1990s,
646 Climate Dynamics, 51, 443–455, doi:10.1007/s00382-017-3933-1.

647 Isobe, A. (2004), Driving mechanism of band structure of mean current over the
648 continental shelf, Journal of Physical Oceanography, 34, 1839–1855.

649 Isobe, A. (2008), Recent Advances in Ocean-Circulation Research on the Yellow Sea
650 and East China Sea Shelves, Journal of Oceanography, 64, 569-584.

651 Jacox, M. G. (2019), Marine heatwaves in a changing climate, Nature, 571, 485–
652 487, doi: 10.1038/d41586-019-02196-1.

653 Kanamitsu, M., W. Ebisuzaki, J. Woollen, S.-K. Yang, J. J. Hnilo, M. Fiorino, and G.
654 L. Potter (2002), NCEP–DOE AMIP-II Reanalysis (R-2), Bulletin of the American
655 Meteorological Society, 83, 1631–1644, doi:10.1175/BAMS-83-11-1631

656 Lee, S.-S., Y.-W. Seo, K.-J. Ha, and J.-G. Jhun (2013), Impact of the western North
657 Pacific subtropical high on the East Asian monsoon precipitation and the Indian
658 Ocean precipitation in the boreal summertime, Asia-pacific Journal of Atmospheric
659 Sciences, 49, 171–182. doi:10.1007/s13143-013-0018-x.

660 Lozovatsky, I. D., Z. Liu, and H. J. S. Fernando (2007a), Tides and mixing in the
661 northwestern East China Sea. Part I: Rotating and reversing tidal flows, Continental
662 Shelf Research, 28(2), 318-337, doi:10.1016/j.csr.2007.08.006.

663 Lozovatsky, I. D., Z. Liu , and H. J. S. Fernando (2007b), Tides and mixing in the
664 northwestern East China Sea, Part II: Near-bottom Turbulence, Continental Shelf
665 Research, 28(2), 338-350, doi:10.1016/j.csr.2007.08.007.

666 Ma, C., D. X. Wu, X. Lin, J. Yang, and X. Ju (2010), An open-ocean forcing in the
667 East China and Yellow seas, Journal of Geophysical Research, 115, C12056,
668 doi:10.1029/2010JC006179.

669 Matsumura, S., S. Sugimoto, and T. Sato (2015), Recent intensification of the western
670 Pacific subtropical high associated with the East Asian summer monsoon, Journal of
671 Climate, 28, 2873–2883, doi:10.1175/JCLI-D-14-00569.1.

672 Mellor, G. L., and T. Yamada (1982), Development of a turbulence closure model for
673 geophysical fluid problems, Review of Geophysics, 20, 851– 875.

674 Menemenlis D, Campin JM, Heimbach P, Hill C, Lee T, Nguyen A, Schodlok M,
675 Zhang H (2008), ECCO2: high resolution global ocean and sea ice data synthesis.
676 Mercat. Ocean Q. Newsl 31:13–21.

677 Mills K. E, A. J. Pershing, C. J. Brown Curtis, Y. Chen, F.-S. Chiang, D. S., Holland
678 Daniel, S. Lehuta, J. A. Nye, J. C. Sun, A. C., Thomas, and R. A. Wahle Richard
679 (2012), Lessons from the 2012 ocean heatwave in the Northwest Atlantic,
680 Oceanography, 26, 60–64.

681 Naimie, C. E., C. A. Blain and D. R. Lynch (2001), Seasonal mean circulation in the
682 Yellow Sea-a model-generated climatology, Continental Shelf Research, 21, 667-695.

683 Ninomiya, K. (2004), Large- and mesoscale features of Meiyu-Baiu front associated
684 with intense rainfalls. pp. 404–435. doi:10.1142/9789812701411_0011.

685 Oey, L.-Y., M.-C. Chang, Y.-L. Chang, Y.-C. Lin, and F.-H. Xu (2013), Decadal
686 warming of coastal China Seas and coupling with winter monsoon and currents,
687 Geophysical Research Letters, 40, 6288–6292, doi:10.1002/2013GL058202.

688 Olita, A., R. Sorgente, A. Ribotti, S. Natale, and S. Gaberšek (2006), Effects of the
689 2003 European heatwave on the Central Mediterranean Sea surface layer: a numerical
690 simulation, Ocean Science, 3, 85–125.

691 Oliver, E. C. J., J. A. Benthuysen, N. L. Bindoff, A. J. Hobday, N. J. Holbrook, C. N.
692 Munday, and S. E. Perkins-Kirkpatrick (2017), The unprecedented 2015/16 Tasman
693 Sea marine heatwave, Nature Communication, 8, 16101.

694 Oliver, E. C. J., M. G. Donat, M. T. Burrows, P. J. Moore, D. A. Smale, L. V.
695 Alexander, J. A. Benthuysen, M. Feng, A. Sen Gupta, A. J. Hobday, N. J. Holbrook, S.
696 E. Perkins-Kirkpatrick, H. A. Scannell, S. C. Straub, and T. Wernberg (2018), Longer
697 and more frequent marine heatwaves over the past century, Nature Communications,
698 9, doi:10.1038/s41467-018-03732-9.

699 Oliver, E. C. J. (2019), Mean warming not variability drives marine heatwave trends,
700 Climate Dynamics, doi:10.1007/s00382-019-04707-2.

701 Oppenheim, A. V, R. W. Schafer, and J. R. Buck (1999), Discrete-time Signal
702 Processing (2Nd Ed.). Prentice-Hall, Inc., Upper Saddle River, NJ, USA.

703 Park C., and C., S. D. Schubert (1994), On the Nature of the 1994 East Asian Summer
704 Drought, Journal of Climate, 10, 1056-1070.

705 Park, S., and P. C. Chu (2007), Synoptic distributions of thermal surface mixed layer
706 and thermocline in the southern Yellow and East China Seas, Journal of
707 Oceanography, 63, 1021–1028.

708 Park, K.A., E. Y. Lee, E. Chang, and S. Hong (2015), Spatial and temporal variability
709 of sea surface temperature and warming trends in the Yellow Sea, Journal of Marine
710 Systems, 143, 24–38.

711 Paulson, C. A., and J. J. Simpson (1977), Irradiance measurements in the upper ocean,
712 Journal of Physical Oceanography, 7, 952–956.

713 Reynolds, R. W., T. M. Smith, C. Liu, D. B. Chelton, K. S., Casey, and M. G. Schlax
714 (2007), Daily high-resolution-blended analyses for sea surface temperature, Journal of
715 Climate, 20(22), 5473–5496, doi:/10.1175/2007JCLI1824.1.

716 Saha, S., S. Moorthi, X. Wu, J. Wang, S. Nadiga, P. Tripp, D. Behringer, Y.-T. Hou,
717 H. Chuang, M. Ek Iredell, J. Meng, R. Yang, M. P. Mendez, H. van den Dool, Q.
718 Zhang, W. Wang, M. Chen, and E. Becker (2013), The NCEP Climate Forecast
719 System Version 2, Journal of Climate, 27, 2185–2208.
720 doi:10.1175/JCLI-D-12-00823.1

721 Saha, S., and coauthors (2010a), The NCEP Climate Forecast System Reanalysis,
722 Bulletin of the American Meteorological Society, 91, 1015–1058.

723 Saha, S., and coauthors (2010b), NCEP Climate Forecast System Reanalysis (CFSR)
724 Monthly Products, January 1979 to December 2010.

725 Schlegel R.W., E. C. J. Oliver, S. Perkins-Kirkpatrick, A. Kruger and A. J. Smit
726 (2017), Predominant Atmospheric and Oceanic Patterns during Coastal Marine
727 Heatwaves, Frontier Marine Science, 4:323, doi: 10.3389/fmars.2017.00323.

728 Smagorinsky, J. (1963), General circulation experiments with the primitive equations,
729 I, The basic experiment, Monthly Weather Review, 91: 99~164.

730 Sparnocchia, S., M. E. Schiano, P. Picco, R. Bozzano, and A. Cappelletti (2006), The
731 anomalous warming of summer 2003 in the surface layer of the Central Ligurian Sea
732 (Western Mediterranean), Annales Geophysicae, 24, 443–452.

733 Tan. H., and R. Cai (2018), What caused the record-breaking warming in East China
734 Seas during August 2016 ?, Atmospheric Sciences Letters, 19, e853,
735 doi:10.1002/asl.853.

US Naval Oceanographic Office and the US Naval Ocean Research and Development Activity (1983) DBDB5 (Digital Bathymetric Data Base-5 Minute Grid). US N.O.O., Bay St. Louis, p 329.

Xia, C., F. Qiao, Y. Yang, J. Ma, and Y. Yuan (2006), Three-dimensional structure of the summertime circulation in the Yellow Sea from a wave-tide-circulation coupled model, Journal of Geophysical Research, 111, C11S03, doi:10.1029/2005JC003218.

Xie, S., J. Hafner, Y. Tanimoto, W. T. Liu, H. Tokinaga, and H. Xu (2002), Bathymetric effect on the winter sea surface temperature and climate of the Yellow and East China Seas, Geophysical Research Letters, 29(24), 2228, doi:10.1029/2002GL015884, 2002.

Yeh S.-W. and C.-H Kim (2010), Recent warming in the Yellow/East China Sea during winter and the associated atmospheric circulation, Continental Shelf Research, 30, 1428-1434.

Wang, B., B. Xiang, and J.-Y. Lee (2013), Subtropical High predictability establishes a promising way for monsoon and tropical storm predictions, Proceedings of the National Academy of Sciences of the United States of America, 110, 2718 LP-2722. doi:10.1073/pnas.1214626110

Wang, J., and L.-Y. Oey (2014), Inter-annual and decadal fluctuations of the Kuroshio in East China Sea and connection with

surface fluxes of momentum and heat, Geophysical Research Letters, 41, 8538–8546, doi:10.1002/2014GL062118.

Wang, S., and H. Zuo (2016), Effect of the East Asian Westerly Jet's Intensity on Summer Rainfall in the Yangtze River Valley and Its Mechanism, Journal of Climate, 29, 2395–2406. doi:10.1175/JCLI-D-15-0259.1

760 Xuan, S., Q. Zhang, and S. Sun (2011), Anomalous midsummer rainfall in Yangtze
761 River-Huaihe River valleys and its association with the East Asia westerly jet,
762 Advances in Atmospheric Science, 28, 387–397, doi:10.1007/s00376-010-0111-3.

763 Xuan, J. L., D. J. Huang, F. Zhou, X. Zhu, and X. P. Fan (2012), The role of wind on
764 the detachment of low salinity water in the Changjiang Estuary in summer, Journal of
765 Geophysical Research: Oceans, 117, C10004, doi:10.1029/2012JC008121.

766 Yanagi, T. and S. Takahashi (1993): Seasonal variation of circulations in the East
767 China Sea and the Yellow Sea. Journal of the Oceanographic Society of Japan, 49,
768 491–501.

769 Yang, D. Z., R. X. Huang, B. S., Yin, X. R., H. Y. Chen, J. F. Qi, …Benthuysen, J.-A.
770 (2018). Topographic beta spiral and onshore intrusion of the Kuroshio Current.
771 Geophysical Research Letters, 45, 287–296, doi.org/10.1002/2017GL076614.

772 Yang, J. (2007), An oceanic current against the wind: How does TaiwanIsland steer
773 warm water into the East China Sea, Journal of Physical Oceanography, 37, 2563–
774 2569, doi:10.1175/JPO3134.1.

775 Zhou, T., D. Gong, J. Li, and B. Li (2009), Detecting and understanding the
776 multi-decadal variability of the East Asian Summer Monsoon Recent progress and
777 state of affairs, Meteorologische Zeitschrift, 18, 455–467,
778 doi:10.1127/0941-2948/2009/0396.

779 Zheng P., D. Wu, and X. Lin (2009), the relationship between the Taiwan Warm
780 Current and Tsushima Warm Current, Journal of hydrodynamics, 2009,21(2):212-218,
781 doi: 10.1016/S1001-6058(08)60138-9.

782

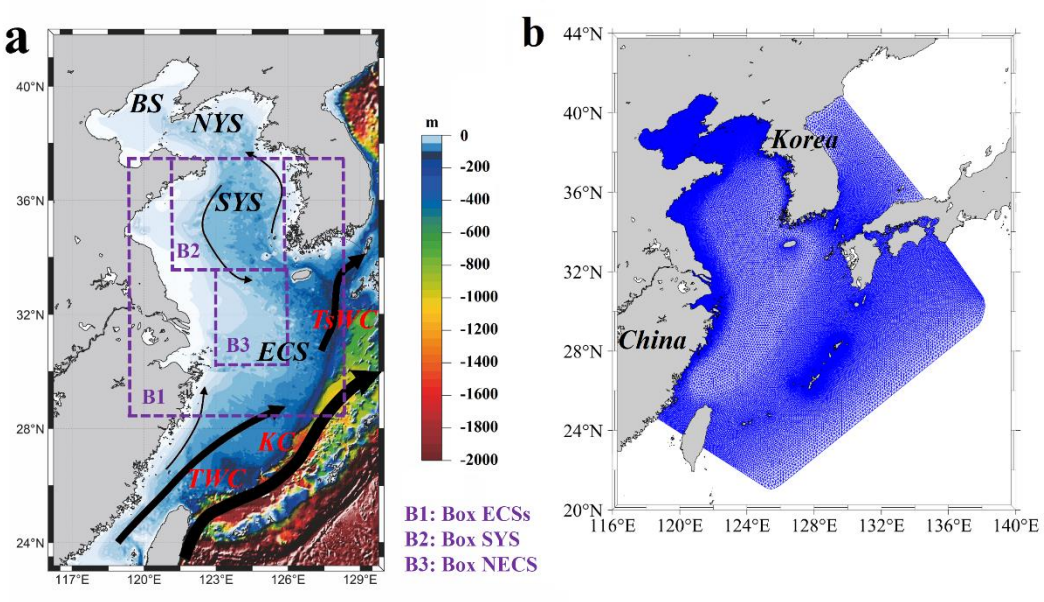

783

784 **Figure 1.** (a) Map of the Bohai Sea (BS), North Yellow Sea (NYS), South Yellow
785 Sea (SYS) and East China Sea (ECS), with topography and main current patterns. (b)
786 The FVCOM-ECSs model domain and mesh grid used in this study. TsWC, TWC and
787 KC represent Tsushima Warm Current, Taiwan Warm Current and Kuroshio Current,
788 respectively. Boxes ECSs (119-126.5°E, 28.75-36.65°N), SYS (121-125.9°E,
789 33.65-37.4°N) and NECS (123-126°E, 30-33.65°N) are indicated in (a) with purple
790 dashed lines, which are the domain where the MHWs are discussed in this study.

791

792

793

794

795

796

797

798

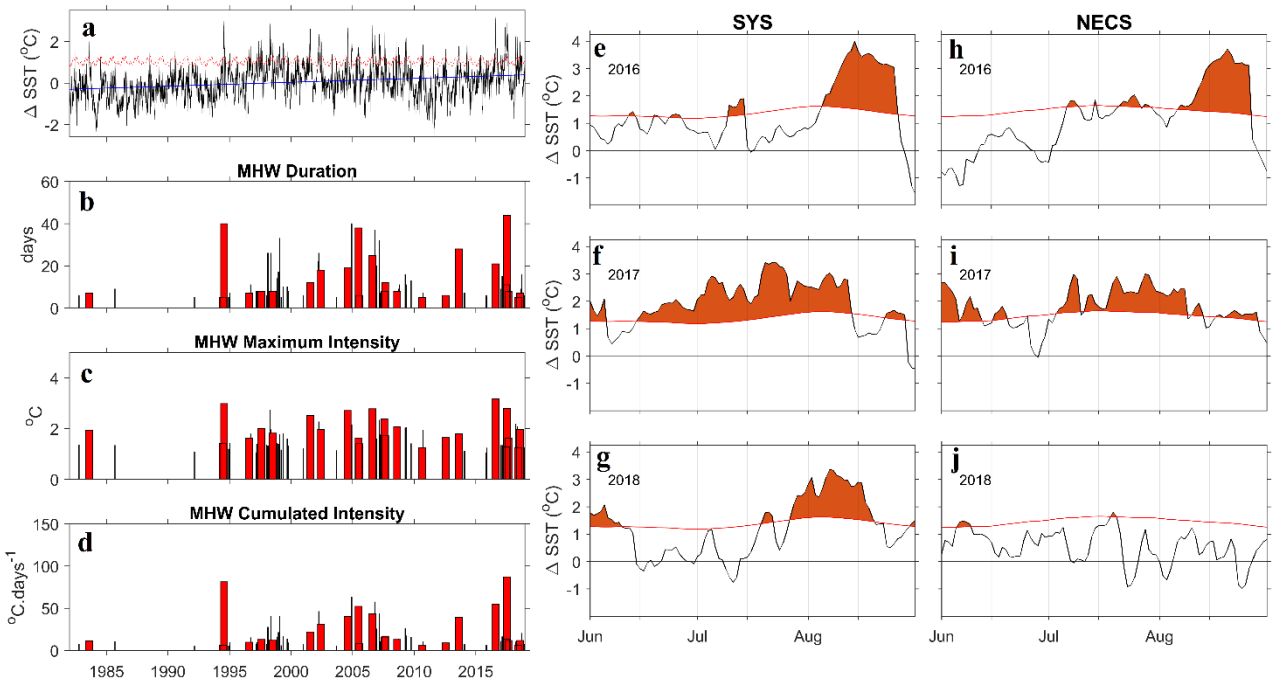

Figure 2. SST and MHW characteristics in the ECSs. (a) Time series of SST anomalies relative to the 1982-2016 climatology. The red and blue lines denote the MHW threshold and a linear trend, respectively. (b) MHW duration (c) maximum intensity and (d) Cumulated intensity during 1982-2018. MHWs occurring in summer (June-August) were plotted in red. (e-j) Zoomed-in SST anomalies during the (top) 2016, middle) 2017,

and (bottom) 2018 summer averaged in the (e-g) SYS and (h-j) NECS box, respectively (Figure1a). MHW threshold (orange line) and SST anomalies exceeding the MHW threshold value (shading) were denoted.

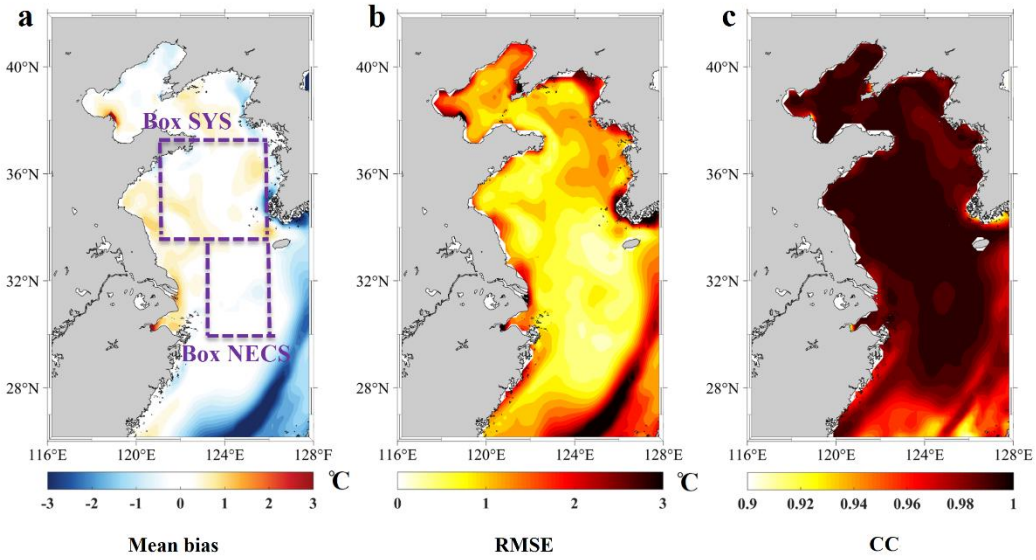

Figure 3. Statistical comparison between the FVCOM-ECSs modeled and satellite SST on monthly time scale from January 2013 to August 2018: (a) mean bias (model - satellite); (b) root mean square error and (c) correlation coefficient. The FVCOM-ECSs outputs were first interpolated onto the NOAA OISST grid before the mean bias, RMSE (Root Mean Square Error) and correlation coefficients between satellite and the FVCOM-ECSs SST were computed. The FVCOM-ECSs SST was taken from the temperature output from the first sigma layer.

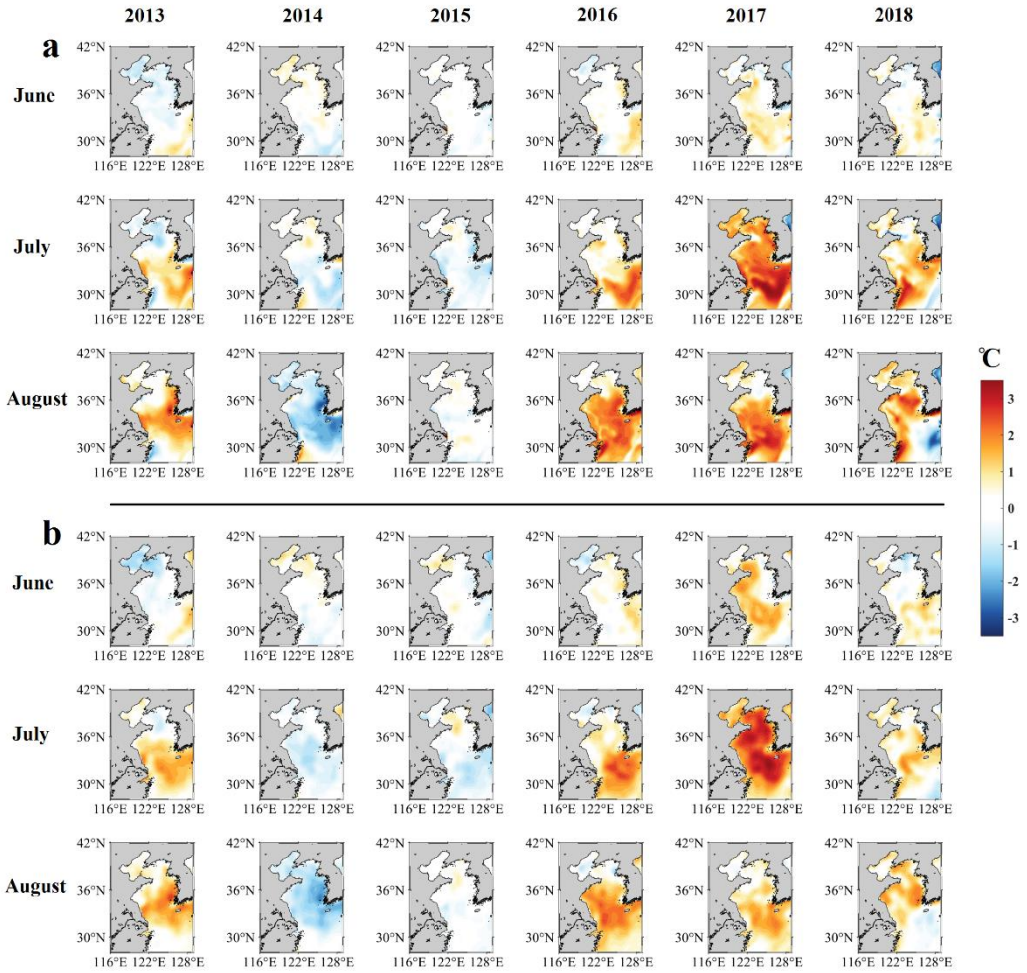

Figure 4. (a) The FVCOM-ECSs modeled and (b) satellite SST anomalies in the ECSs in June, July and August during 2013-2018.

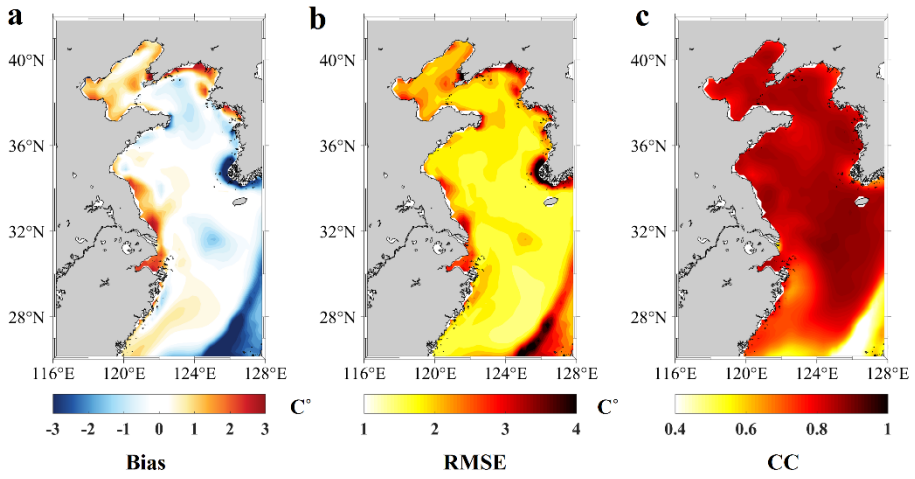

Figure 5. Statistical comparison between the FVCOM-ECSs modeled and satellite SST on daily time scale in JJA from 2013 to 2018: (a) mean bias (model - satellite); (b) root mean square error and (c) correlation coefficient.

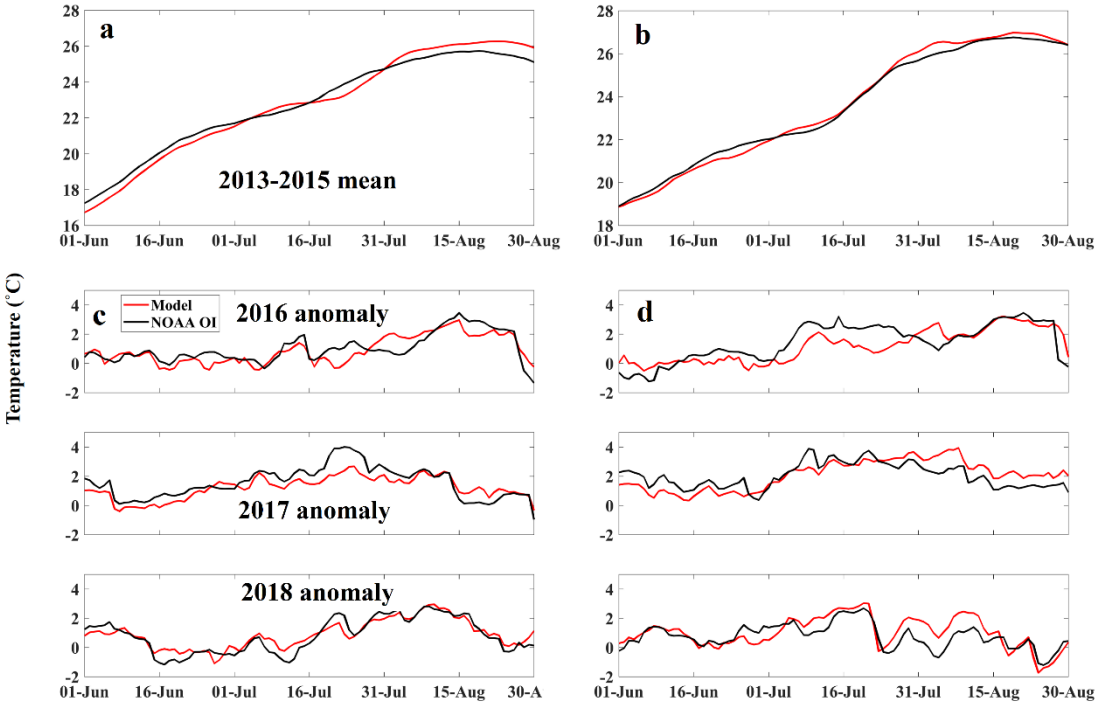

847

848 **Figure 6.** Comparison of normal-year (2013-2015) averaged and anomalous

849 (2016-2018) SST during JJA for Boxes SYS (a,c) and NECS (b,d).

850

851

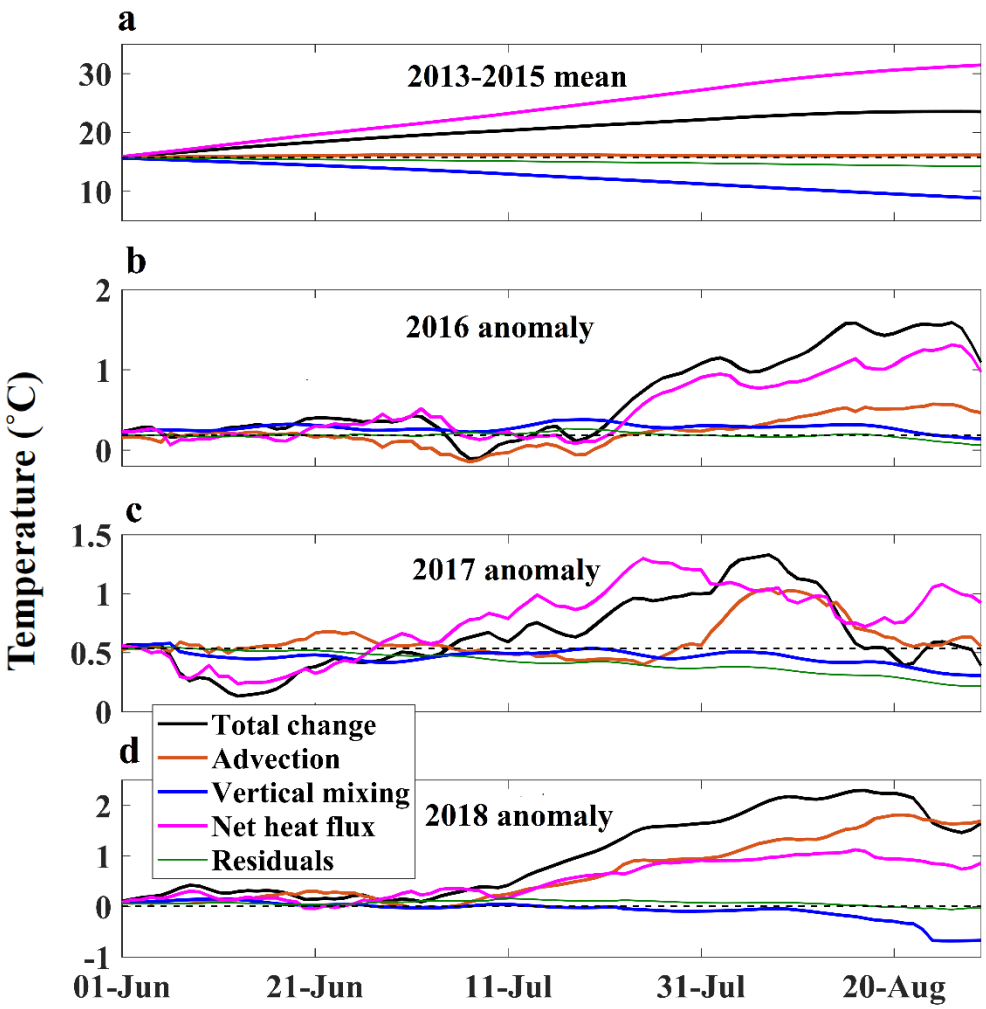

852

853 **Figure 7.** (a) Normal-year averages (2013-2015) and (b-d) anomalies (2016-2018) of
854 temperature at the top 20 m for Box SYS in JJA caused by individual terms. Thin
855 dash black lines indicate the temperature in (a) or temperature anomalies in (b) on
856 July 1st.

857

858

859

860

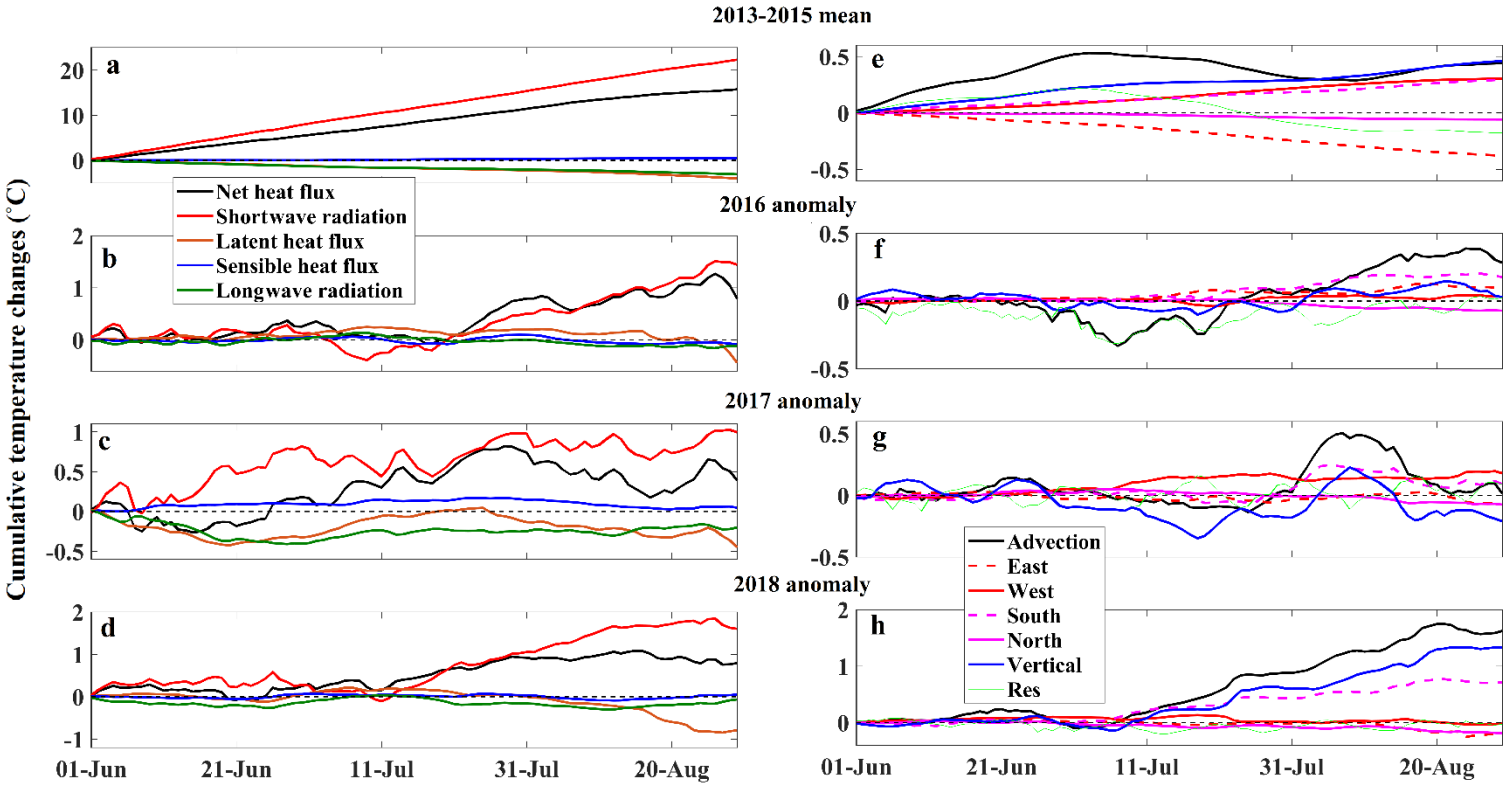

861

862 **Figure 8.** (a) Normal-year averages (2013-2015) and (b-d) anomalies (2016 -2018) of cumulative temperature changes from June 1st at the top

863 20 m for Box SYS in JJA caused by each heat flux terms. (e) Normal-year averages and (f-h) anomalies of cumulative temperature changes from

864 June 1st at the top 20 m for Box SYS caused by advection at various boundaries. Thin dash black lines indicates 0˚C.

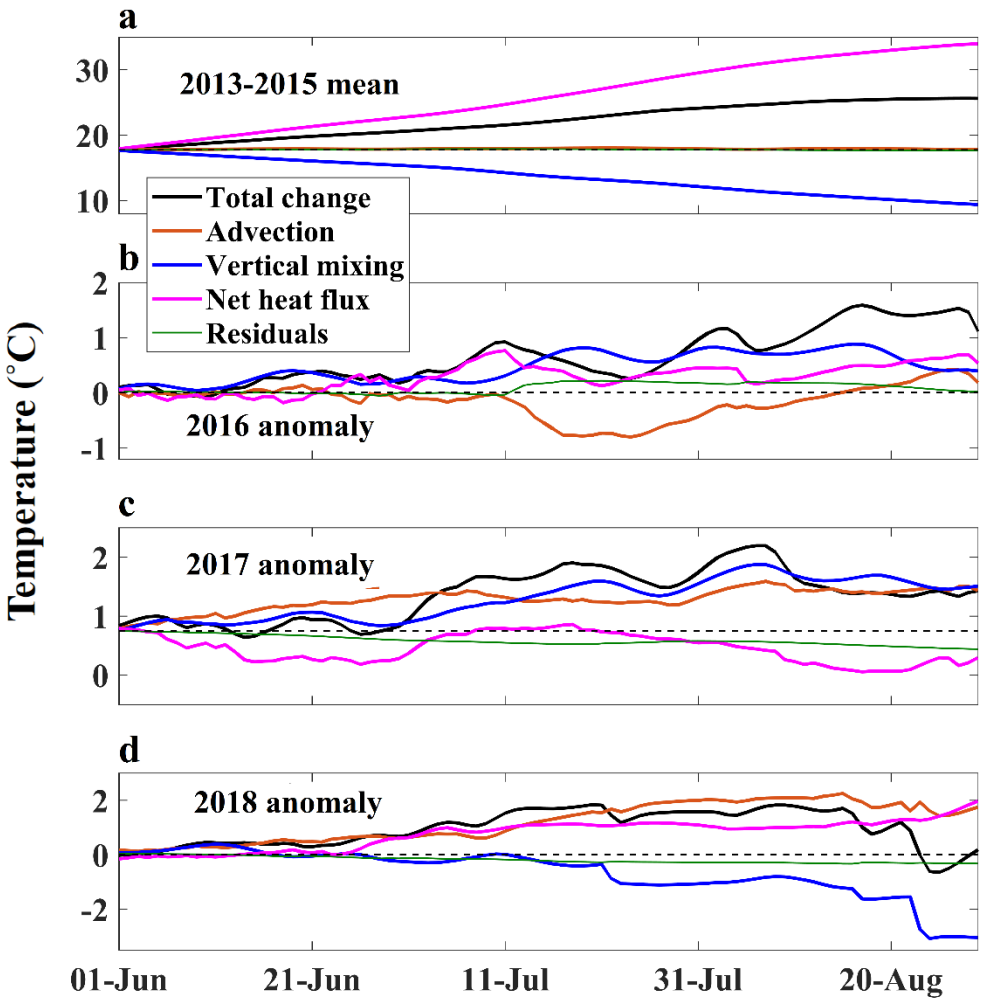

865

866 **Figure 9.** As in Figure 7 but for Box NECS.

867

868

869

870

871

872

873

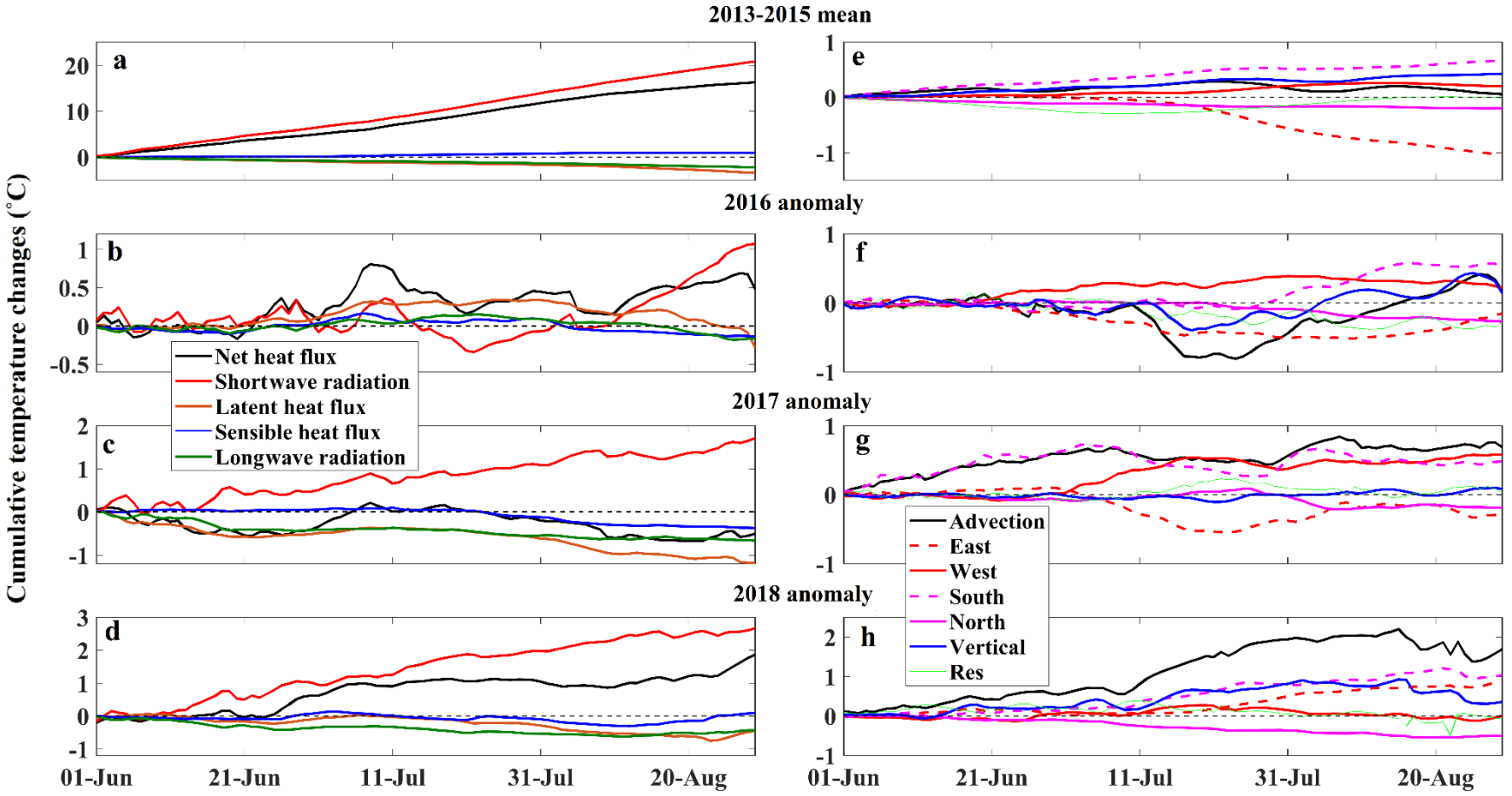
2013-2015 mean
2016 anomaly
2017 anomaly
2018 anomaly
Cumulative temperature changes (°C)
a
b
c
d
e
f
g
h
Net heat flux
Shortwave radiation
Latent heat flux
Sensible heat flux
Longwave radiation
Advection
East
West
South
North
Vertical
Res
01-Jun
21-Jun
11-Jul
31-Jul
20-Aug

874

875 **Figure 10.** As in Figure 8 but for Box NECS.

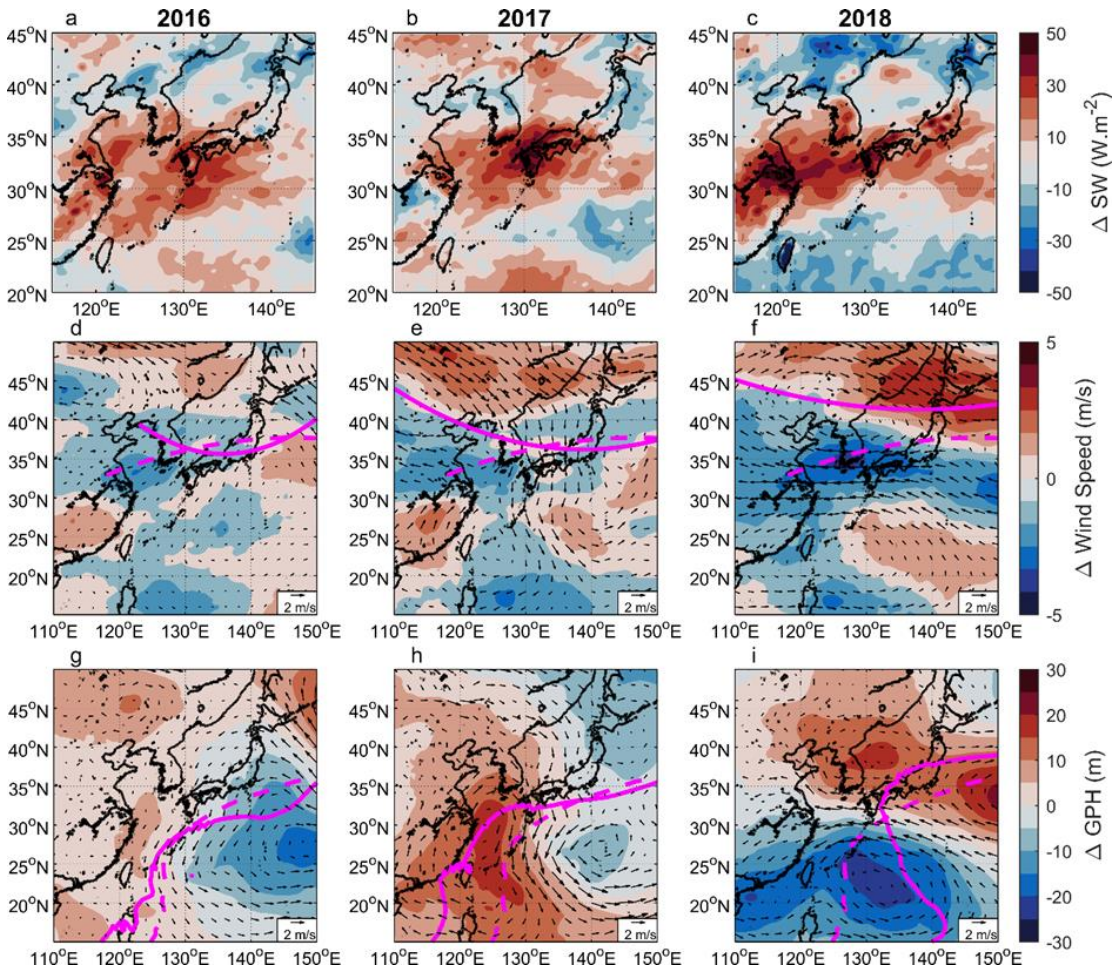

Figure 11. Drivers of shortwave radiation anomalies. (a-c) Surface shortwave radiation anomalies averaged during the 2016-2018 summers (JJA). (d-f) 500hPa wind speed (shading) and wind direction (vectors) anomalies. The climatological (dashed) and averaged (solid) position of the 500hPa Jet is plotted in magenta. (g-i) 850hPa geopotential height (shading) and wind (vectors) anomalies. The climatological (dashed) and averaged (solid) position of the 1490 geopotential height contour is plotted in magenta. The 2013-2015 normal years JJA averages were defined as the climatology.

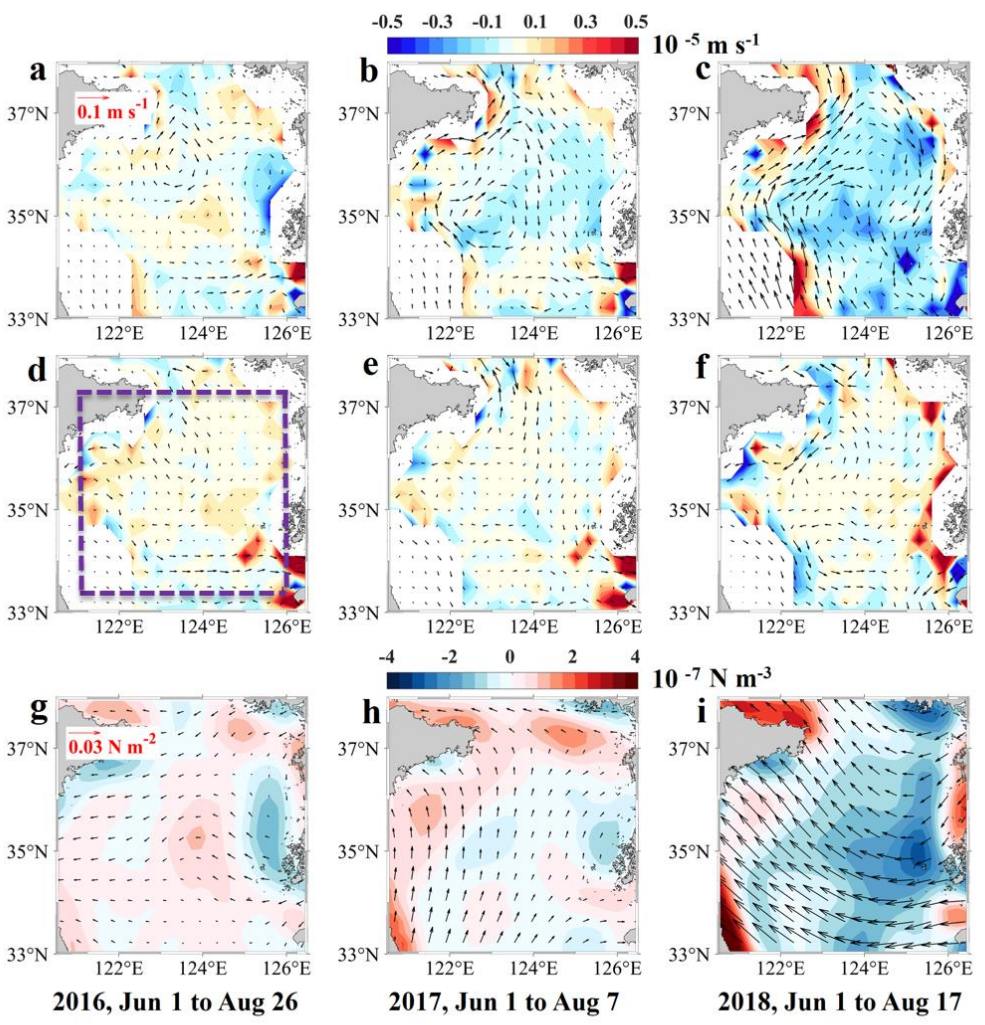

Figure 12. (a-c) Anomalies of horizontal (vectors) and vertical (contour) currents averaged during periods from June 1st to the day of maximum temperature anomalies of JJA in each year (2016-2018) for Box SYS. (d-f) As in (a-c) but for the simulation

891 driven by averaged winds during normal years (2013-2015). (g-i) Anomalies of wind stress (vectors) and stress curl (contour)
892 averaged during corresponding periods in (a-c). The horizontal currents are averaged for the top 20 m and the vertical currents
893 are at 20 m.

894

895

896

897

898

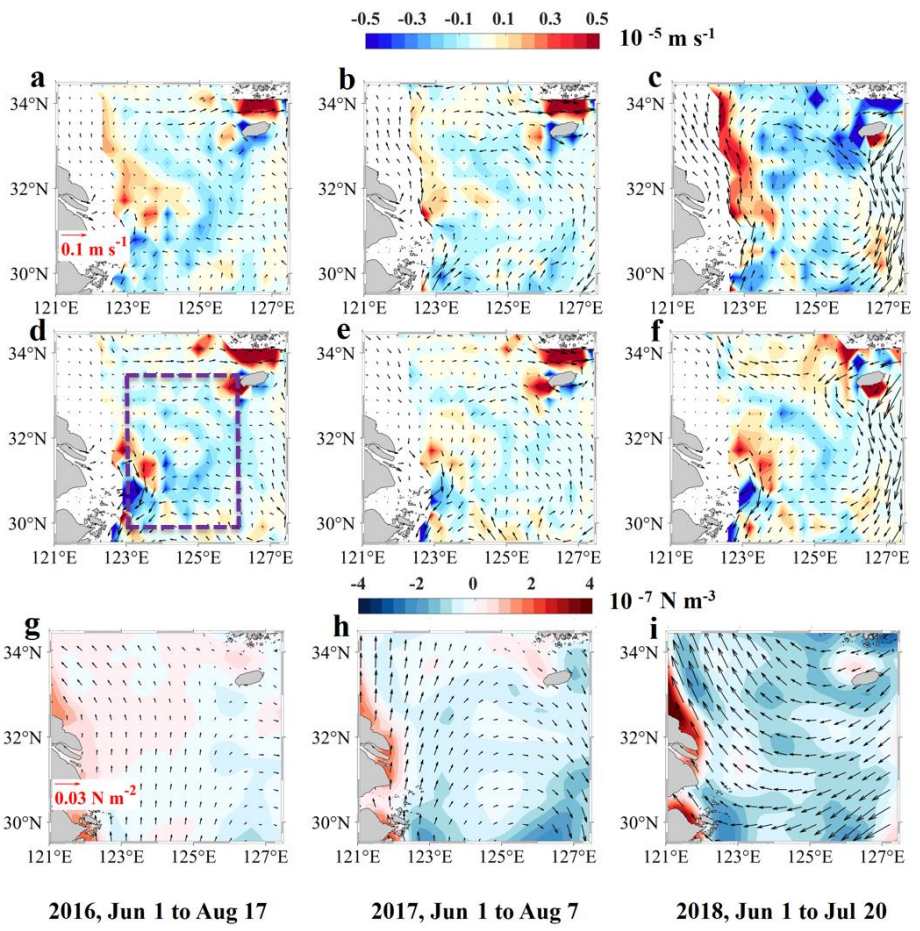

899

900 **Figure 13**. As in Figure 12 but for Box NECS

901

902

903

904

905

906

907

908

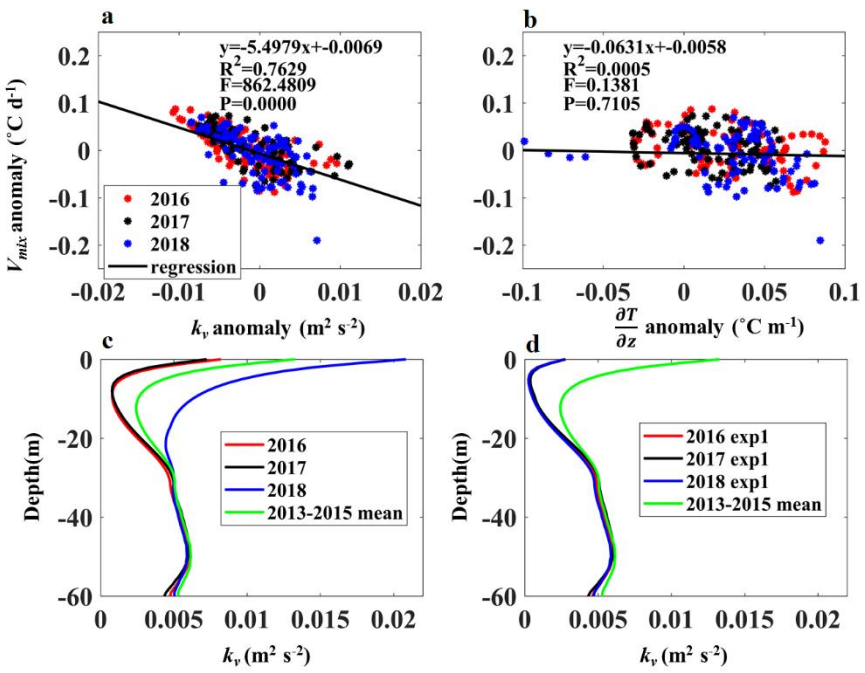

Figure 14. Anomalies (2016 to 2018) of daily temperature changes due to vertical mixing are plotted against the anomalies of daily-averaged (a) vertical eddy viscosities and (b) vertical temperature gradients at 20 m in Box NECS. (c) Vertical profile of JJA-mean vertical eddy viscosities in Box NECS. (d) As in (c) but for experiment 1. 2013-2015 mean vertical eddy viscosities in (d) were same as that in (c). The corresponding statistic estimators are also given in (a) and (b).

Figure 1.

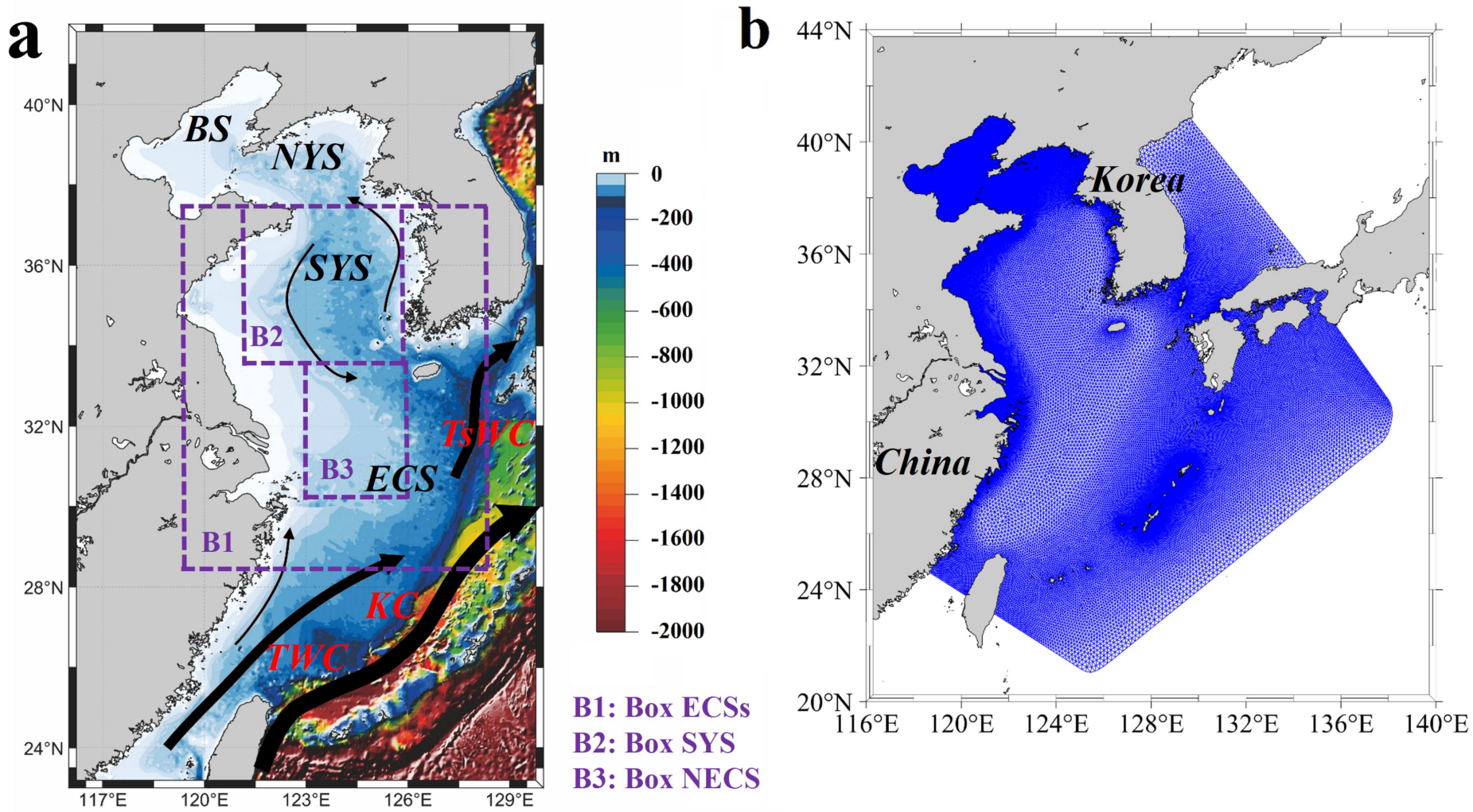
a
BS
NYS
SYS
B2
B3
ECS
B1
TsWC
KC
TWC
40°N
36°N
32°N
28°N
24°N
117°E
120°E
123°E
126°E
129°E
m
0
-200
-400
-600
-800
-1000
-1200
-1400
-1600
-1800
-2000
B1: Box ECSs
B2: Box SYS
B3: Box NECS
b
Korea
China
44°N
40°N
36°N
32°N
28°N
24°N
20°N
116°E
120°E
124°E
128°E
132°E
136°E
140°E

Figure 2.

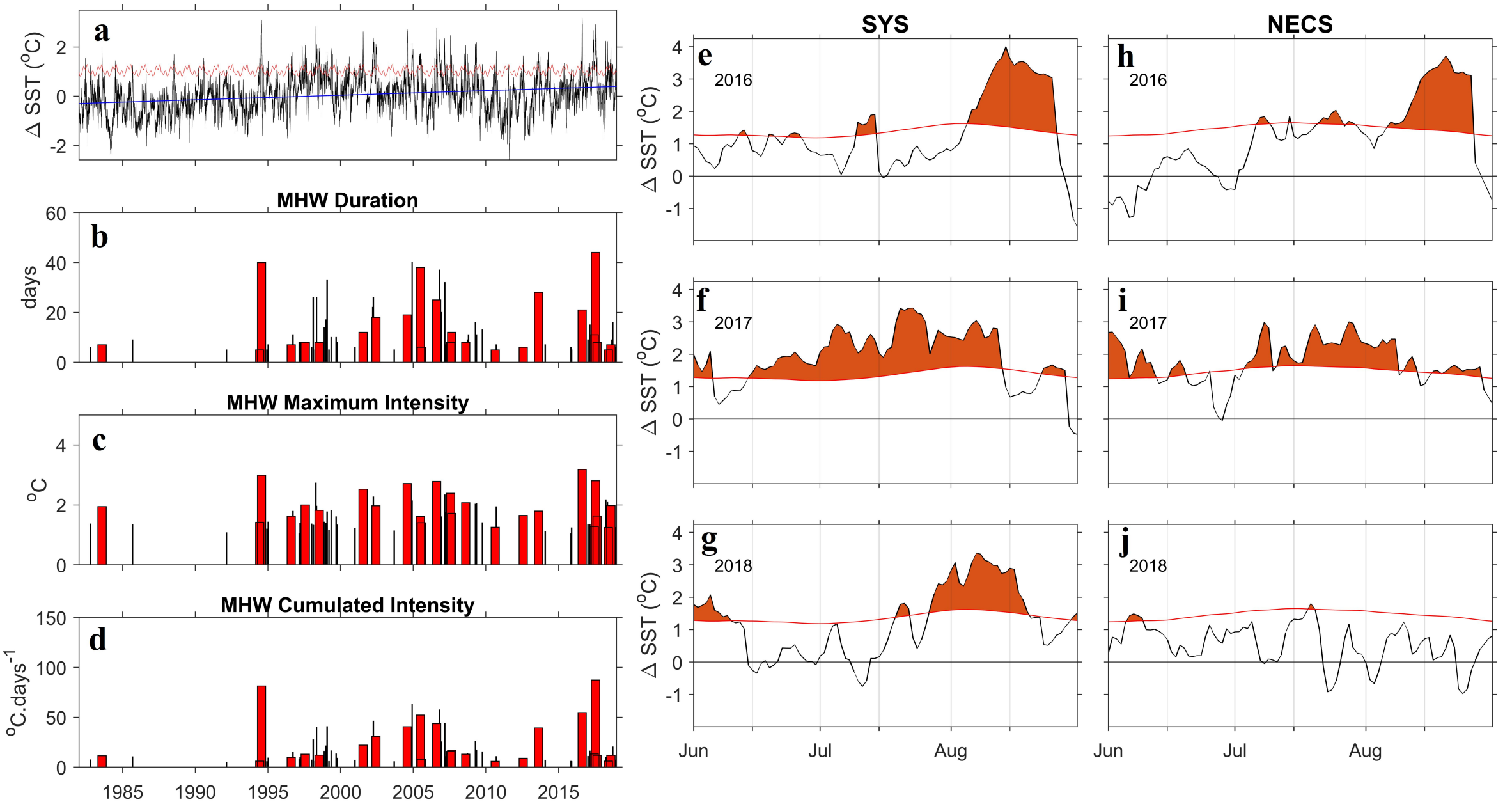
a
Δ SST (°C)
MHW Duration
b
days
MHW Maximum Intensity
c
°C
MHW Cumulated Intensity
d
°C.days-1
1985
1990
1995
2000
2005
2010
2015
SYS
NECS
e
2016
h
2016
f
2017
i
2017
g
2018
j
2018
Jun
Jul
Aug

Figure 3.

a

b

c

Box SYS

Box NECS

40°N

36°N

32°N

28°N

116°E

120°E

124°E

128°F

128°E

℃

-3 -2 -1 0 1 2 3

0 1 2 3

0.9 0.92 0.94 0.96 0.98 1

Mean bias

RMSE

CC

Figure 4.

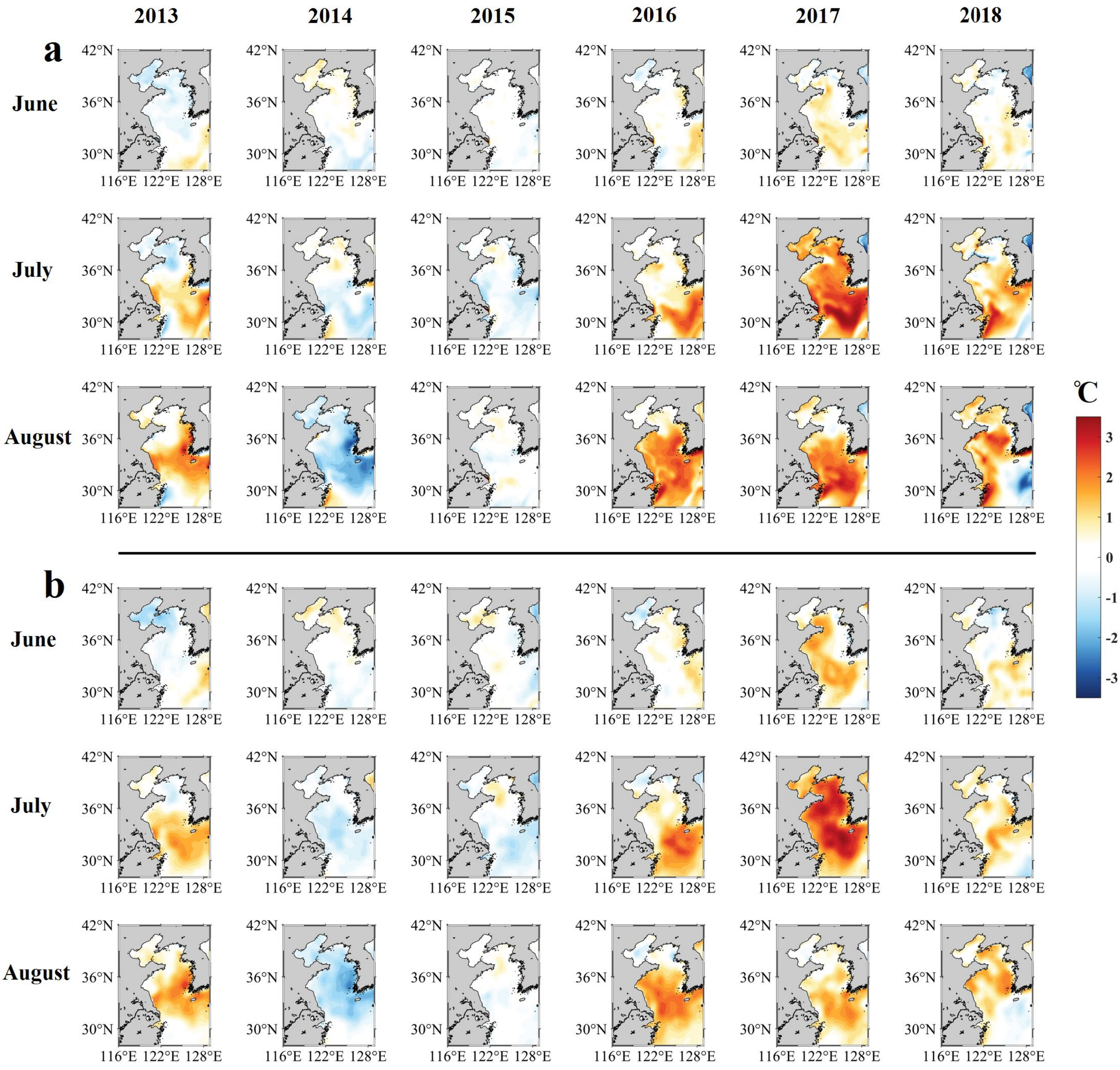
2013
2014
2015
2016
2017
2018
a
June
July
August
b
June
July
August
42°N
36°N
30°N
116°E 122°E 128°E
℃
3
2
1
0
-1
-2
-3

Figure 5.

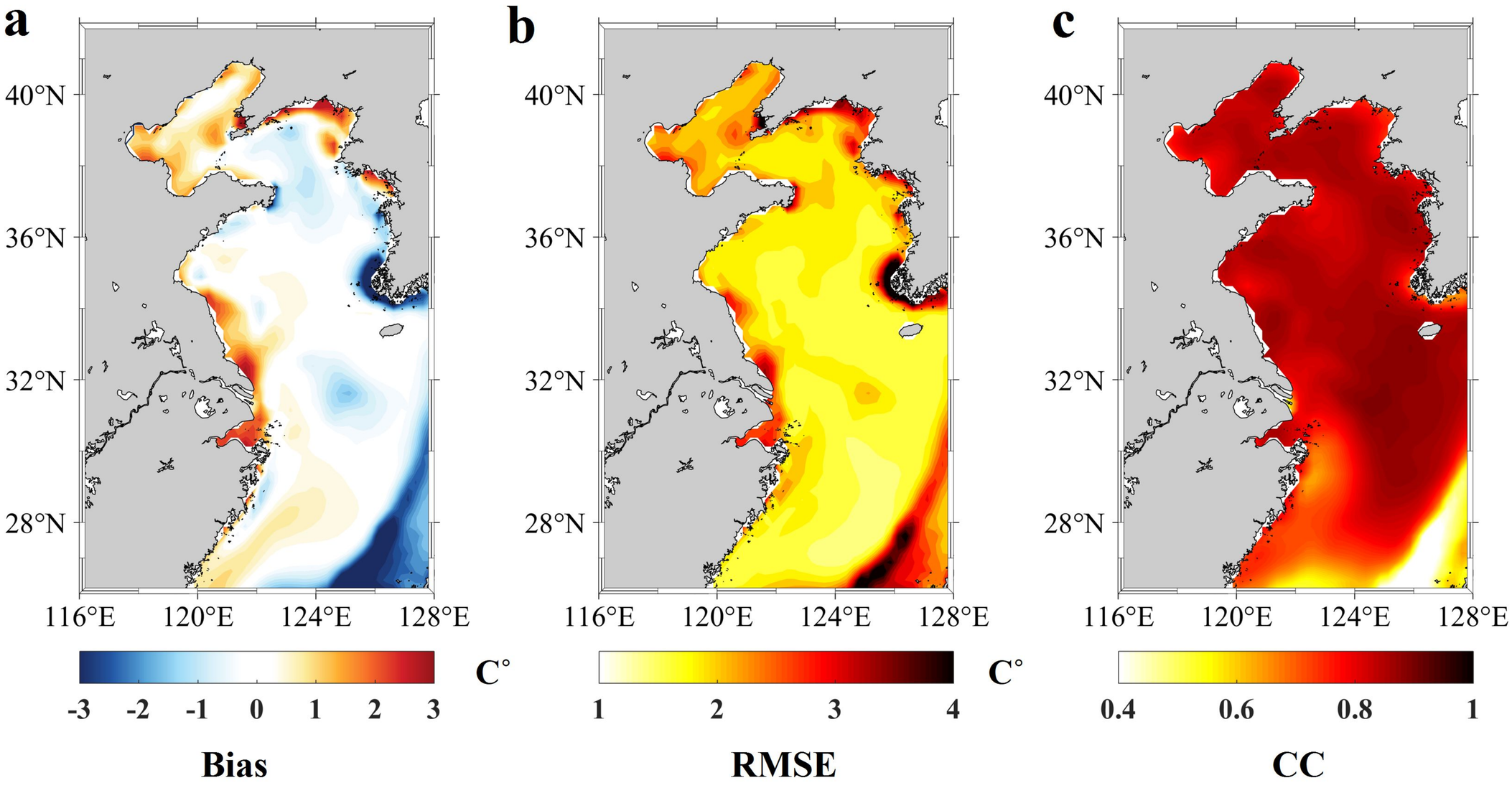
a
b
c
40°N
36°N
32°N
28°N
116°E
120°E
124°E
128°E
-3
-2
-1
0
1
2
3
C°
Bias
1
2
3
4
C°
RMSE
0.4
0.6
0.8
1
CC

Figure 6.

a

2013-2015 mean

b

c

Model
NOAA OI

2016 anomaly

d

2017 anomaly

2018 anomaly

Temperature (°C)

28
26
24
22
20
18
16
4
2
0
-2

01-Jun
16-Jun
01-Jul
16-Jul
31-Jul
15-Aug
30-Aug

Figure 7.

a

2013-2015 mean

30
20
10

b

2016 anomaly

2
1
0

Temperature (°C)

c

2017 anomaly

1.5
1
0.5
0

d

2018 anomaly

2
1
0
-1

Total change
Advection
Vertical mixing
Net heat flux
Residuals

01-Jun
21-Jun
11-Jul
31-Jul
20-Aug

Figure 8.

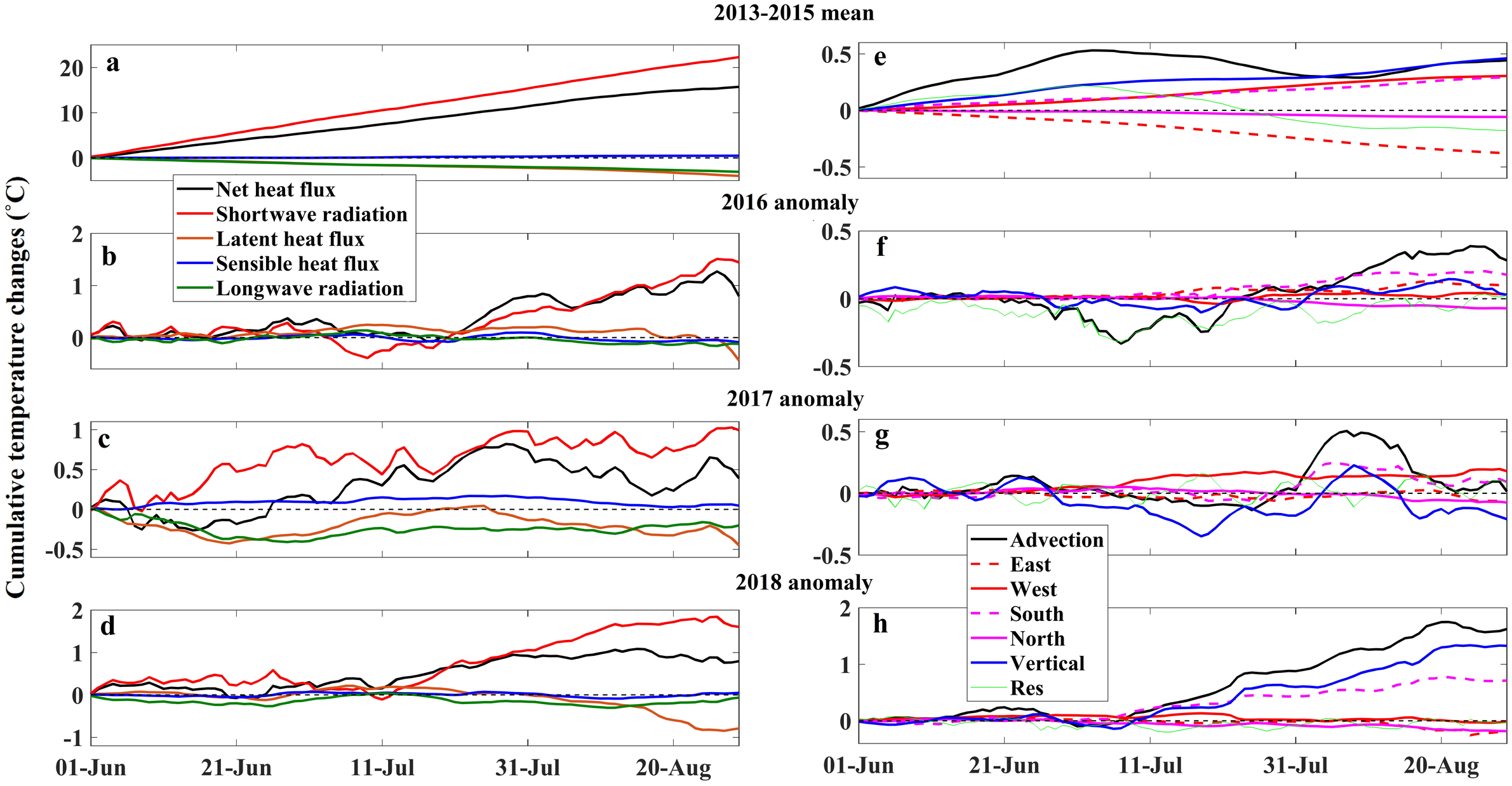
2013-2015 mean
2016 anomaly
2017 anomaly
2018 anomaly
Cumulative temperature changes (°C)
a
b
c
d
e
f
g
h
Net heat flux
Shortwave radiation
Latent heat flux
Sensible heat flux
Longwave radiation
Advection
East
West
South
North
Vertical
Res
01-Jun
21-Jun
11-Jul
31-Jul
20-Aug

Figure 9.

a

2013-2015 mean

30
20
10

Total change
Advection
Vertical mixing
Net heat flux
Residuals

b

2016 anomaly

2
1
0
-1

Temperature (°C)

c

2017 anomaly

2
1
0

d

2018 anomaly

2
0
-2

01-Jun
21-Jun
11-Jul
31-Jul
20-Aug

Figure 10.

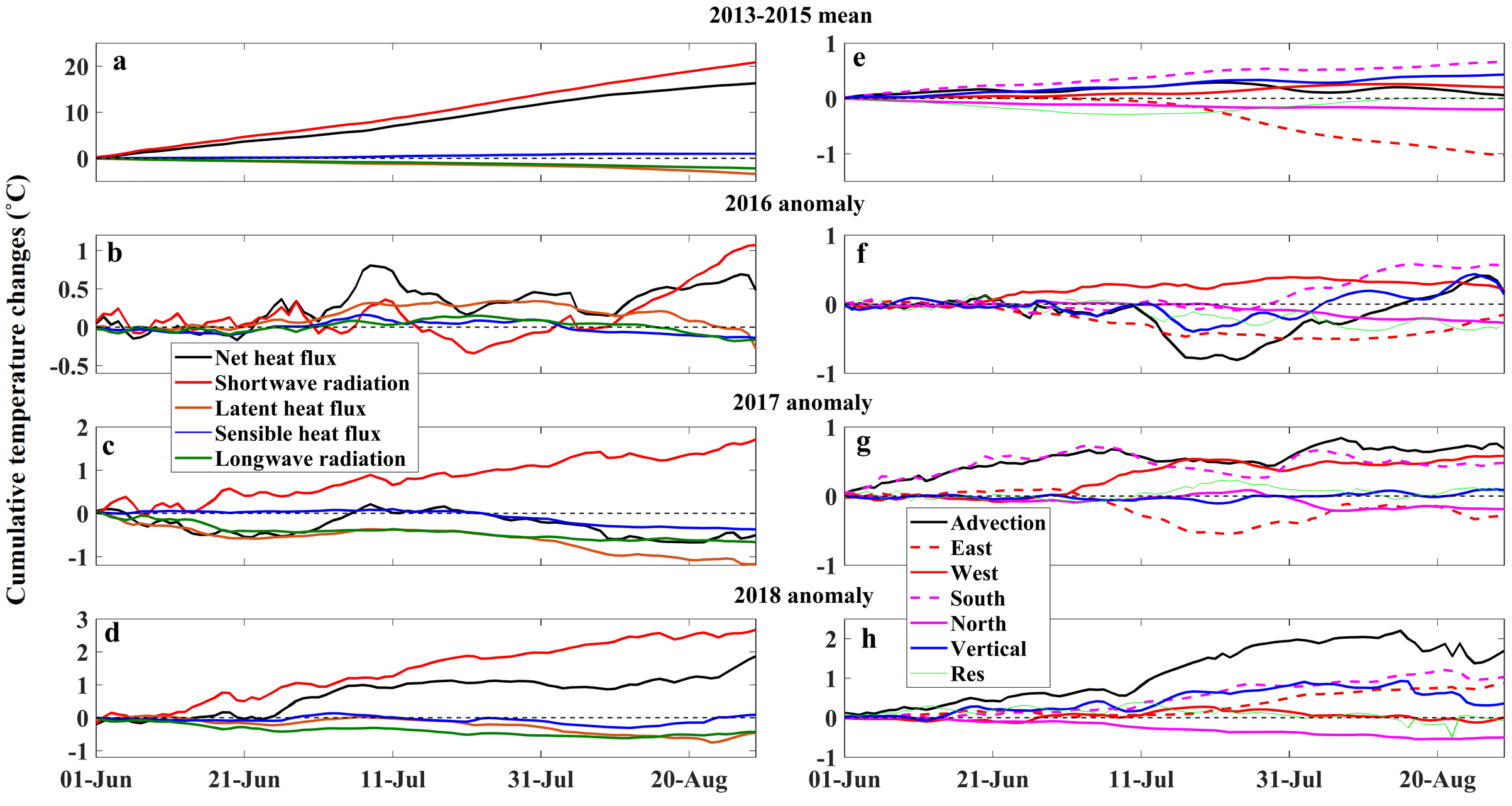
2013-2015 mean
2016 anomaly
2017 anomaly
2018 anomaly
Cumulative temperature changes (°C)
a
b
c
d
e
f
g
h
Net heat flux
Shortwave radiation
Latent heat flux
Sensible heat flux
Longwave radiation
Advection
East
West
South
North
Vertical
Res
01-Jun
21-Jun
11-Jul
31-Jul
20-Aug

Figure 11.

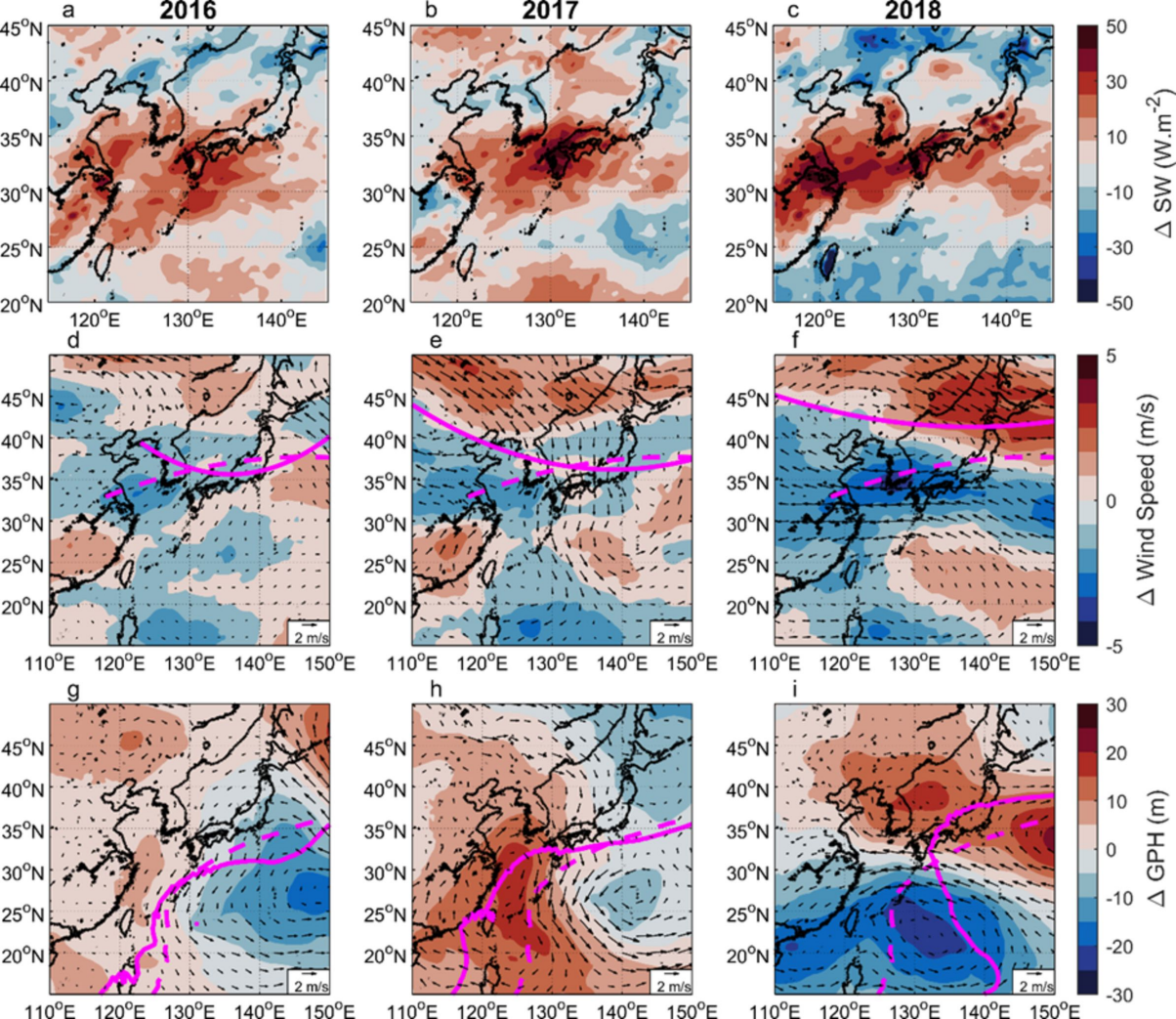
a
2016
b
2017
c
2018
45°N
40°N
35°N
30°N
25°N
20°N
120°E
130°E
140°E
Δ SW (W.m-2)
50
30
10
-10
-30
-50
d
e
f
110°E
150°E
2 m/s
Δ Wind Speed (m/s)
5
0
-5
g
h
i
Δ GPH (m)
30
20
10
0
-10
-20
-30

Figure 12.

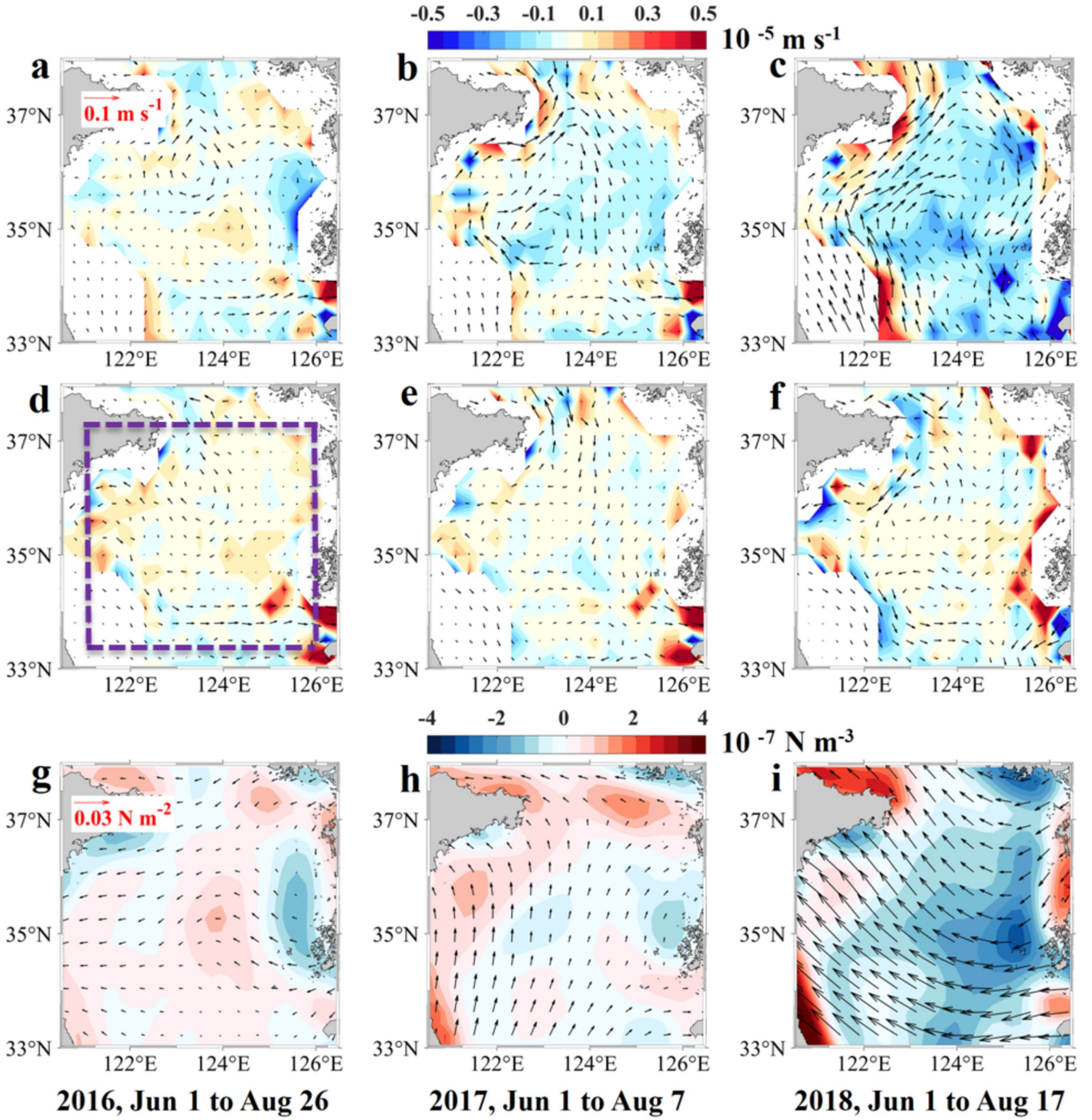
-0.5 -0.3 -0.1 0.1 0.3 0.5
10 -5 m s-1
a
b
c
d
e
f
0.1 m s-1
37°N
35°N
33°N
122°E
124°E
126°E
-4 -2 0 2 4
10 -7 N m-3
g
h
i
0.03 N m-2
2016, Jun 1 to Aug 26
2017, Jun 1 to Aug 7
2018, Jun 1 to Aug 17

Figure 13.

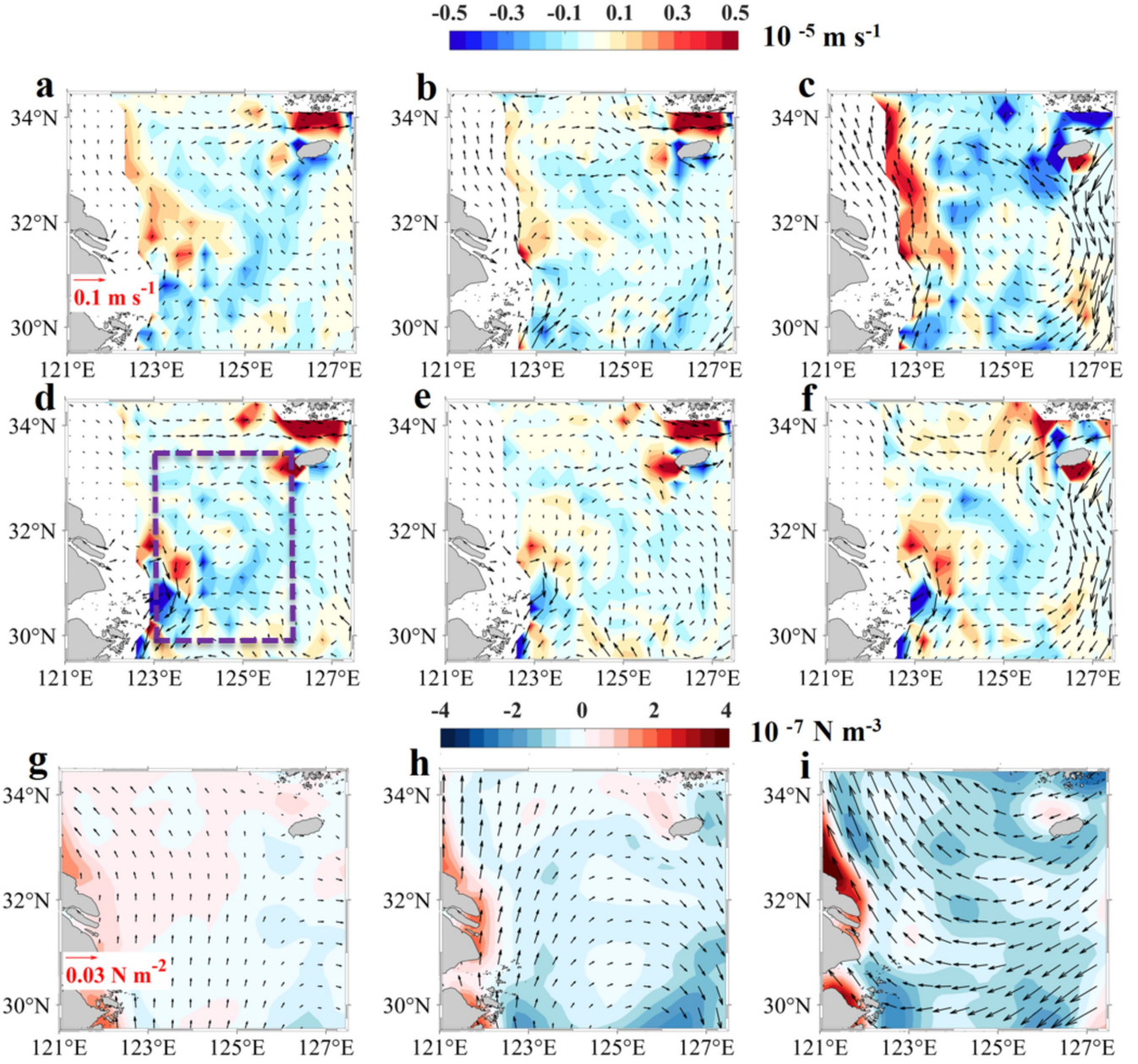
-0.5 -0.3 -0.1 0.1 0.3 0.5
10 -5 m s-1
a
b
c
d
e
f
g
h
i
34°N
32°N
30°N
121°E
123°E
125°E
127°E
0.1 m s-1
-4 -2 0 2 4
10 -7 N m-3
0.03 N m-2
2016, Jun 1 to Aug 17
2017, Jun 1 to Aug 7
2018, Jun 1 to Jul 20

Figure 14.

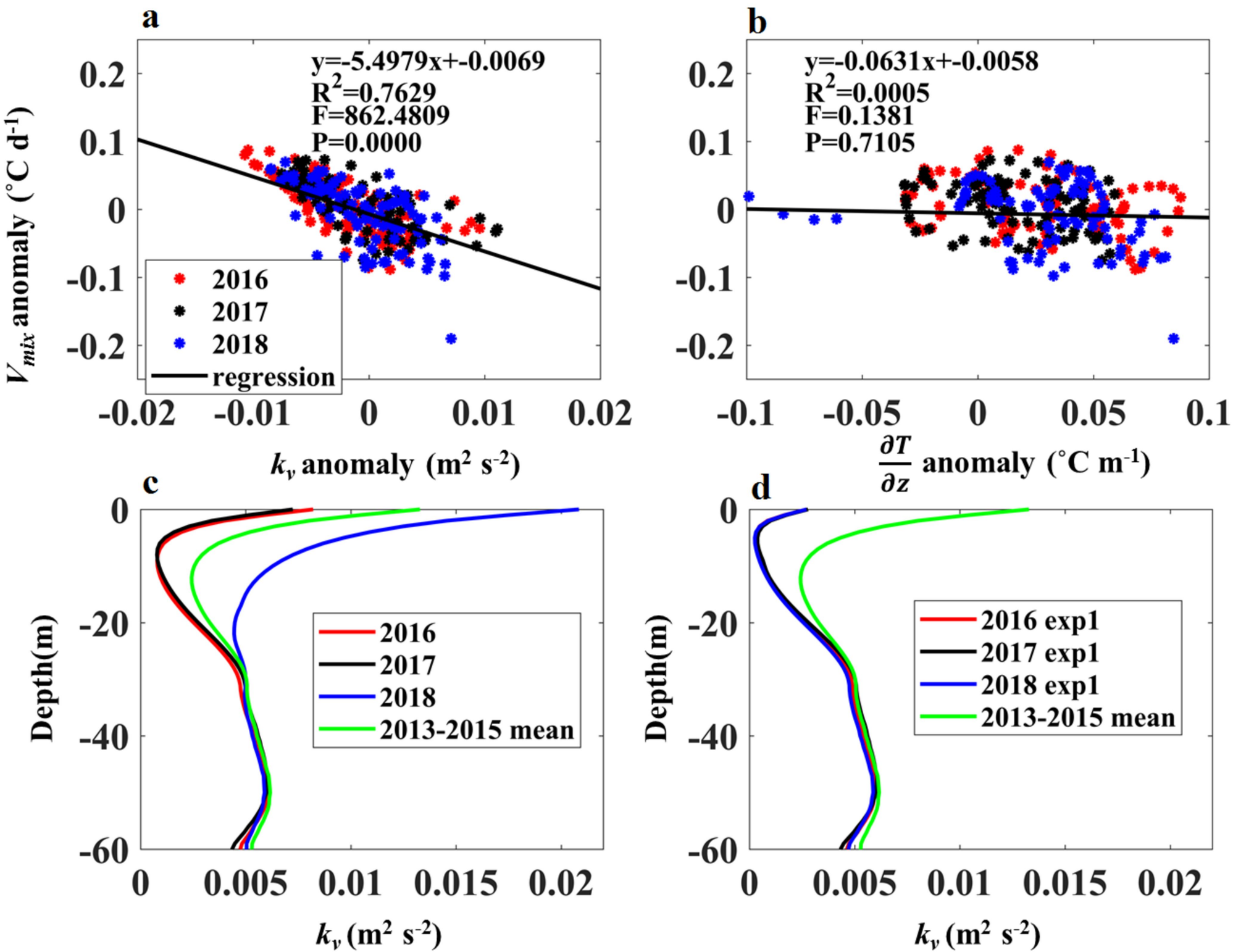
a
y=-5.4979x+-0.0069
R²=0.7629
F=862.4809
P=0.0000
2016
2017
2018
regression
V_{mix} anomaly (°C d⁻¹)
b
y=-0.0631x+-0.0058
R²=0.0005
F=0.1381
P=0.7105
c
k_v anomaly (m² s⁻²)
Depth(m)
2016
2017
2018
2013-2015 mean
k_v (m² s⁻²)
d
$\frac{\partial T}{\partial z}$ anomaly (°C m⁻¹)
2016 exp1
2017 exp1
2018 exp1
2013-2015 mean